5-2009

Behavior of Prestressed Concrete Bridge Girders

Franklin B. Angomas
Utah State University

BEHAVIOR OF PRESTRESSED CONCRETE BRIDGE GIRDERS

by

Franklin B. Angomas

A thesis submitted in partial fulfillment
of the requirements for the degree

of

MASTER OF SCIENCE

in

Civil and Environmental Engineering

Approved:

_____	_____
Paul J. Barr Major Professor	Marvin W. Halling Committee Member
_____	_____
James A. Bay Committee Member	Byron R. Burnham Dean of Graduate Studies

UTAH STATE UNIVERSITY
Logan, Utah
2009

ABSTRACT

Behavior of Prestressed Concrete Bridge Girders

by

Franklin Angomas, Master of Science

Utah State University, 2009

Major Professor: Dr. Paul J. Barr
Department: Civil and Environmental Engineering

For this research, prestress losses were monitored in six HPC bridge girders. These measured losses were compared to predicted losses according to four sources. Prestress loss predictive methods considered for this research were: 1- AASHTO LRFD 2004, 2- AASHTO LRFD 2004 Refined, 3- AASHTO LRFD 2007, and 4- AASHTO LRFD Lump Sum method. On the other hand, the camber prediction methods used in the present research were: 1- Time dependent method described in NCHRP Report 496, 2- PCI multiplier method, and 3- Improved PCI Multiplier method. For the purpose of this research, long-term prestress losses were monitored in select girders from Bridge 669 located near Farmington, Utah. Bridge 669 is a three-span prestress concrete girder bridge. The three spans have lengths of 132.2, 108.5, and 82.2 feet long, respectively. Eleven AASHTO Type VI precast prestressed girders were used to support the deck in each span. The deflection of several girders from a three-span, prestressed, precast concrete girder bridge was monitored for 3 years. Fifteen bridge girders were fabricated for the three span-bridge. Ten girders from the exterior spans had span length of 80 feet,

and five girders from the middle span had span length of 137 feet. From the results of this research, in both the 82- and 132-foot-long, the AASHTO LRFD 2004 Refined Method does a better job predicting the prestress loss and it can be concluded that all the prediction methods do a better job predicting the loss for the larger girders. The Lump Sum method predicted very accurately the long term prestress loss for the 132-foot-long girders.

(109 pages)

DEDICATION

This thesis is dedicated to my mother, for her unconditional support during these past two years and without whom I would not be where I am today. To my family, friends, and all other that motivated me throughout all this process. The gratitude I have for the inspiration and confidence conferred upon me by these people is indescribable.

Franklin B. Angomas

ACKNOWLEDGMENTS

I would like to thank my committee members, Drs. Paul Barr, for all the guidance and support, James Bay, and Marv Halling, for their support and insight throughout this process. Finally, I would like to thank UDOT, Eagle Precast, and Geneva Rock for the concrete samples on which the majority of this research was performed.

Franklin B. Angomas

CONTENTS

Page

LIST OF TABLES

LIST OF FIGURES

CHAPTER 1

INTRODUCTION

1.1 Context

The use of High Performance Concrete is common among the US DOTs for short to medium span prestress concrete girder bridges. Therefore the designer should understand thoroughly how prestressed HPC girders behave. Accurate prediction of deflections and prestress losses are crucial in a cost-effective design. In order to accurately predict the HPC prestressed girder behavior, a correct materials characterization is imperative, since prestress loss and deflection calculations depend on material properties.

For this research, prestress losses were monitored in six HPC bridge girders. These measured losses were compared to predicted losses according to four sources. Prestress loss predictive methods considered for this research were: 1- AASHTO LRFD 2004, 2- AASHTO LRFD 2004 Refined, 3- AASHTO LRFD 2007, and 4- AASHTO LRFD Lump Sum method. Additionally, the camber prediction methods used in the present research were: 1- Time dependent method described in NCHRP Report 496, 2- PCI Multiplier Method, and 3- Improved PCI Multiplier method.

1.2 Prestress Loss

Accurate prediction of the long-term, prestress losses in concrete bridge girders is an important part of the design process. An overprediction in the prestress loss could mean a limitation of the span length of the girder, and a considerable increase in the

prestressing force required to overcome such losses. On the other hand, an under-prediction of the prestress losses could translate into undesired deflections and cracking under service conditions. Because in many concrete bridge girders, the cracking control under service loads is the controlling parameter in the design process, a precise but safe prestress loss prediction method is imperative.

Prestress losses can be defined as the decrease in the initial prestressing force. There are two main types of prestress losses depending on the time and duration of their occurrence; the first is the instantaneous elastic shortening loss. The second type is the long-term losses, mostly due to relaxation of the prestressing strands and creep and shrinkage of the concrete. Prestress losses are also influenced by other time-dependent concrete properties, like its compressive strength and its modulus of elasticity.

1.3 Deflections

Prestressed concrete members are typically more slender than reinforced concrete members. Because of this attribute, the prediction of deflections requires special consideration. For prestressed concrete girders, designed to be fully prestressed, an emphasis must be made to the upward deflection, or camber. Since shrinkage and creep are inherent properties of concrete, this camber may increase with time due to these properties. Excessive camber of bridge girders, may result in an invasion of the girder in the road profile, or an irregular surface, in addition, the effects of the permanent dead load and live load to the final midspan deflection must be investigated to guarantee the members serviceability.

The application of a prestress force, in a simply supported beam, will cause upward camber. Creep, shrinkage, and steel relaxation produce a reduction in the camber due to the initial prestress. Conversely the creep has a dual effect, because creep strains in the concrete tends to increase the negative curvature associated with prestress and, therefore, increase the camber.

While prediction of camber may be difficult, due to the time-dependents factors mentioned above, good models are available for calculating the effects of creep and shrinkage on concrete, which permits the calculation of deflections within acceptable ranges of accuracy.

1.4 Research Objectives

The objectives of this research are, first, to investigate the accuracy of the prestress loss prediction methods presented in the AASHTO LRFD Specification and compare them to the prestress loss data acquired by instrumenting six concrete girders on Bridge 669 pertaining to the Legacy Highway, near Layton, Utah. Second, to investigate the accuracy of the deflections predictions methods presented in both NCHRP Report 496 and PCI manual, and compare it to measured deflections on the SR18/SR516 Bridge overpass in the state of Washington.

1.5 Organization of Thesis

The organization of the thesis is as follows: Chapter 2 presents a literature review. A description of the tests performed to the concrete is presented in Chapter 3. Chapter 4

investigates the accuracies of the distinctive prediction methods for both prestress loss and deflections. A summary and conclusions are presented in Chapter 5.

CHAPTER 2

LITERATURE REVIEW

2.1 Investigation of Long-Term Prestress Losses in Pre-tensioned High Performance Concrete Girders

Waldron (2004) motivated his research based on the fact that the efficient prediction of long-term prestress losses is imperative in the design of prestressed concrete bridges. An over-prediction of prestress losses may result in an excessively conservative design for service load stresses, and an under-prediction of the prestress losses, can result in cracking when the service loads are applied. Shrinkage and creep generate the most substantial time-dependent effect on the loss of prestress.

For this research HPC girders, with design compressive strengths ranging from 8,000 psi to 10,000 psi, and three 8,000 psi lightweight HPC (HPLWC) girders were instrumented to determine the changes in strain and prestress losses. The author used several creep and shrinkage models to evaluate the instrumented girders. The author of this dissertation found that for the HPLWC, each model overpredicted the long-term strains, and the Shams and Kahn model was the best predictor of the measured strains and for the normal weight HPC, the models under-estimated the measured strains at early ages and overestimated the measured strains at later ages, and the B3 model was the best-predictor of the measured strains. The PCI-BDM model was the most consistent model across all of the instrumented girders.

For this dissertation the shrinkage and creep properties of the HPC mixtures were measured in the laboratory and compared to the creep and shrinkage models available.

The author found that the best predictor of creep strains in the Dismal Swamp Bridge was the AASHTO LRFD model; meanwhile the best predictor for the shrinkage strain was the GL2000 model. The best predictor of the overall shrinkage was the PCI-BDM model. All the models correlated to high-strength concrete. The PCI-BDM, NCHRP 496, and Shams and Kahn predicted the total strain better than the traditional models. In addition, the PCI-BDM model was the only model to predict accurately enough in both normal an high strength concrete.

Based on the results obtained from the studies performed at Pinner's Point and Dismal Swamp, the PCI-BDM model is the best predictor of the average, total, long-term strains associated with these HPC mixtures, and in general, the more recent models developed for high-strength concrete predicts the long-term strains better than the traditional models.

The HPLWC shows different behavior when compared to the creep and shrinkage models than does the normal weight HPC investigated. The models all overestimate the measured strains of both the HPLWC test girders and the Chickahominy River Bridge girders. The Shams and Kahn model is the best predictor of the strains measured in the HPLWC bridge girders, predicting the average strain of the bridge girders reasonably well. The PCI-1975 model predicts strains that produce a reasonable lower bound for the measured strains for the HPLWC bridge girders, and is the best overall predictor of the strains for the HPLWC test girders.

For the normal weight HPC girders investigated in the scope of this research, the models have a propensity to under predict the measured strains at early ages and over-predict the measured strains at later ages. The B3 and AFREM models are the best

predictors for both sets of the Pinner's Point girders, and in general, the models that account for compressive strength predict the strains of the 10,000 psi girders better than the strains of the 8,000 psi girders. Also, since both sets of girders from the Pinner's Point Bridge exhibit similar strains, it is likely that the models accounting for compressive strength would predict the strains of the 8,000 psi girders better by assuming a 10,000 psi compressive strength. This indicates that compressive strength is not the best property to use to adjust the long-term models for HPC; however, it is a simple parameter to measure and is generally known at the design stage, which is why it is used by each of the recently developed models. Finally, for the Dismal Swamp girders, the B3 model is the best predictor of the measured strains.

In general, when probing the girders from all the bridges, the researchers concluded that no model consistently predicts the strains of each set of girders. The PCI-BDM model is the only model to be ranked in the top half of the 10 models for all of the bridge girders, demonstrating that it is the most consistent predictor of the measured strains over the whole observed period. Examining the strains at the end of the modeled period as an approximation of the strains at the end of service life, the PCI-BDM and NCHRP 496 models are the best predictors for the normal weight HPC girders and the Shams and Kahn and PCI-1975 model are the best predictors for the HPLWC girders. Finally the research concludes that is clear from this comparison that a single model is not well suited to both lightweight and normal weight HPC without some modification for lightweight concrete.

Recommendations given by the author for further investigation:

1. The NCHRP 496 Refined and Approximate methods for estimating prestress losses are recommended for estimating the prestress losses at the end of service life for girders utilizing normal weight HPC similar to that used in this study. Continued use of the AASHTO Standard and LFRD Specifications is overly conservative but acceptable until the NCHRP 496 methods are adopted by AASHTO.
2. Further investigation of the HPLWC is needed. The measured strains in the HPLWC girders varied by approximately 200 microstrain from girder to girder, which is more than twice the variation between girders seen with the normal weight HPC. This is likely due to variations in the concrete batches because of the precaster's unfamiliarity with the lightweight aggregates used in the concrete mixture.
3. In the interim, the NCHRP 496 Refined and Approximate methods can be used to conservatively estimate the total losses for girders utilizing the HPLWC analyzed in this study.
4. Further investigation of the early age behavior of the normal weight HPC analyzed in this study is needed. For the normal weight HPC considerably more strain was measured prior to 30 days after transfer than predicted by the models. The elastic shortening strains (determined from measurements taken two to four hours after detensioning) were also larger than the elastic strains estimated from the measured concrete properties.
5. Further investigation of the behavior of the bridge girders after deck placement is also needed. Each instrumented girder exhibited a nearly flat strain curve prior to

deck placement indicating that creep and shrinkage had nearly ceased. However, after deck placement instead of exhibiting decreasing compressive strains, as would be caused by creep recovery and differential shrinkage, the girders showed increasing compressive strains for a period of approximately 100 days following deck placement.

2.2 Prestress Losses in Pre-tensioned High-Strength Concrete Bridge Girders (NCHRP Report 496)

The main purpose of the NCHRP Report 496 by Tadros et al. (2003) was to provide the bridge designers with guidelines for the prediction of prestress losses in high strength pretensioned concrete girders. These guidelines are intended to deal with the limitations of the AASHTO LRFD Specifications currently in use. The researchers focused their improvements in two main subjects: the first, the modulus of elasticity prediction methods, with emphasis in high strength concrete and second, prestress losses prediction models that take into consideration the time dependant effects of creep and shrinkage, especially in high strength concretes, where creep and shrinkage tend to be lower.

This research was composed of experimental and theoretical programs. The experimental portion of the research consisted in lab tests in order to characterize the materials and in the measurement of prestress loss in full scale bridge girders in four states, representing with this a wide range of geographical areas and construction practices. Also, the results of previous research in seven states were included in the

report. In addition the results of research carried by American Concrete Institute (ACI) Committee 363 and FHWA were considered.

The girders were instrumented in order to collect strains and temperatures in the concrete. The girders were instrumented at the centroid of the prestressing strands in order to measure the change of strain of the prestressing strands and therefore calculate the loss in the prestressing force. Vibrating wire strain gages were embedded directly in the concrete for these measurements. The data was collected by an automated system consisting of a laptop computer and a data logger.

As a conclusion the researchers proposed a detailed method that uses the aging coefficient approach for computing prestress losses between transfer and casting of decks described by Tadros et al. (2003) in the PCI-BDM for precast non-composite members. The approach was also adopted by the European CEBFIP Recommendations 25. The theory is expanded here to cover composite action between precast concrete girders and cast-in-place deck slabs. The prestress losses of pretensioned members, Δf_pT, consist of the following four components, each of which relates to a significant construction stage:

1. Instantaneous prestress loss due to elastic shortening at transfer, Δf_{pES}.
2. Long-term prestress losses due to shrinkage of concrete, $(\Delta f_{pSR})_{id}$, and creep of concrete, $(\Delta f_{pCR})_{id}$, and relax-ation of prestressing strands, $(\Delta f_{pR2})_{id}$, between the time of transfer and just before deck placement.
3. Instantaneous prestress gain due to the placement of deck weight and SIDL, Δf_{pED}.
4. Long-term prestress losses, between the time of deck placement and the final service life of the structure, due to shrinkage of the girder, $(\Delta f_{pSD})_{df}$, creep of the

girder, $(\Delta f_{pCD1} + \Delta f_{pCD2})_{df}$, relaxation of prestressing strands, $(\Delta f_{pR3})_{df}$, and shrinkage of the deck concrete, $(\Delta f_{pSS})_{df}$. Total prestress losses in pretensioned bridge girders, Δf_{pT}, relative to the stress immediately before transfer is thus given by the equation:

$$\Delta f_{pT} = \Delta f_{pES} + (\Delta f_{pSR} + \Delta f_{pCR} + \Delta f_{pR2})_{id} - \Delta f_{pED} + (\Delta f_{pSD} + \Delta f_{pCD1} + \Delta f_{pCD2} + \Delta f_{pR3} - \Delta f_{pSS})_{df} \quad (2.1)$$

For the prestress loss proposed method the authors made the following assumptions:

1. Prestress losses are calculated for conditions at the maximum positive moment section.
2. No mild steel reinforcement exists at that section.
3. Elastic losses at transfer or elastic gains due to the application of external loads are not considered.
4. Prestress is transferred to the concrete at 1 day in accelerated plant curing conditions.
5. The cast-in-place deck weight (for composite construction) is applied to the precast concrete section without any shoring after at least 28 days from the time of prestress transfer.
6. V/S ratio for the girder cross section is 3 in. to 4 in.

The researchers found that the measured total prestress losses for Nebraska girders G1 and G2 were 31.96 ksi and 35.65 ksi, which are 15.8% and 17.6% of the

actual jacking stress, respectively. The measured total prestress losses for New Hampshire girders G3 and G4 were 43.51 ksi and 42.33 ksi, 21.5% and 20.9% of the actual jacking stress, respectively. The corresponding values for the Texas girder were 25.35 ksi (12.5%) and for the Washington girders were 42.06 ksi (20.8%) and 39.98 ksi (19.7%). The ratios of the total estimated-to-measured prestress losses ranged from 0.84 to 1.27 with an average of 1.00 and a standard deviation of 15%.

The research results led to the conclusion that concrete compressive strength, V/S ratio, curing methods, and time elapsed after the end of curing influence shrinkage. A proposed shrinkage formula produced results that averaged 105% of the measured values, compared to 174% when using the AASHTO-LRFD method and 155% when using the ACI-209 method. Predictions of modulus of elasticity, shrinkage, and creep are influenced by local materials and practices. Therefore, data for local materials and mixture proportions should be used when available.

The proposed approximate method produces better estimates of long-term prestress losses in comparison to those obtained by the AASHTO-LRFD Lump Sum method because the Lump Sum method does not account for the level of prestressing or ambient relative humidity.

2.3 Bridge Prestress Losses in Dry Climate

For this research (Saiidi, Hutchens, and Gardella, 1998) instrumented a box-girder bridge during its construction in southern Nevada. The research was motivated by concerns on the effects that low relative humidity would have on prestress losses. The monitoring period for this bridge was carried over a twenty-four months period. These

measured prestress losses were then compared to four prestress loss prediction models, AASHTO Specifications, ACI, PCI committee report; and Naaman's time step method.

The bridge object of this research was the Greenway Bridge. This bridge is a simply supported, post-tensioned, multi-cell box girder structures with an 18° skew. A 200 mm thick diaphragm separates the cells at midspan. Each girder has two 100 mm diameter ducts containing 19 post-tensioning strands, and one 113 mm duct containing either 26 or 27 strands depending on the girder.

The researchers used the following instrumentation: Four extra tendons, two in the south exterior girder and two in the southernmost interior girder, were placed in the bridge. Three electrical strain gages were bonded to three different wires on each cable for a total of 12 strain gages. On each data collection day, hourly measurements were taken from the strain gages for a period of 24 hours to allow for averaging throughout the day. The electrical strain gage data indicate the total losses due to creep and shrinkage, but do not include effects of relaxation, because relaxation losses are the changes in stress under constant strain.

All of the methods mentioned above account for relative humidity except the PCI method. These methods assume a constant ambient relative humidity. Nonetheless the variations in RH were taken into consideration in this study, in order to carry a regression analysis of the measured strand prestress losses using a logarithmic fit. In order to account for the offset between the instrumented tendons and the centroid of the other tendons, stresses were increased by 14 MPa.

For the Greenway Bridge, the extrapolated measured creep and shrinkage prestress losses were approximately 30% lower than that estimated by using the

AASHTO method. In terms of total loss prediction (excluding elastic shortening), AASHTO was conservative by approximately 20%. The low average ambient humidity did not appear to lead to excessive losses beyond those predicted by the AASHTO code. As a result of this study it was recommended to the NDOT to continue to design prestress concrete bridges in southern Nevada using the AASHTO method. For bridges in northern Nevada, however, losses in excess of AASHTO prediction have been noted due to considerable daily and seasonal variation of RH.

The authors concluded that the comparison between the measured losses and the time – step predictions using the Naaman and the ACI committee 209 showed very close correlation. The PCI method led to considerably lower losses than those measured or determined using the other analytical methods. The measured deflection history of the bridge reflected the variations in prestress force that were affected by climatic changes. The data from a logarithmic fit of the measured deflections showed good agreement with the predicted values, which were based on a time-dependent equation presented by Nilson (1987).

2.4 Comparative Study of Various Creep and Shrinkage Prediction Models for Concrete

This paper by Goel, Kumar, and Paul (2007) summarizes and compares various prediction models developed to predict the creep and shrinkage in concrete. A brief description of the most recent models for prediction of creep and shrinkage is presented in this paper. Among these models are: the ACI-209 R-82 model, the B3 model, the CEB-FIP model code 1990 and the GL2000 model.

The variations of creep and shrinkage in the concrete are time-dependant. These properties (creep and shrinkage) have a considerable negative impact on the final performance of concrete structures. Creep in concrete manifests as a change on the material dimensions under the effect of sustained loads. Furthermore, regardless of a load being applied or not, concrete undergoes a change of dimensions due to drying shrinkage. The authors consider that since both occur simultaneously the treatment of the two together is convenient from a practical point of view. Failure to include creep and shrinkage effects in the analysis of the structures may lead to excessive deformation and wide spread cracking.

The many concrete properties, i.e. compressive strength, age of concrete at loading, type of curing conditions, ambient conditions, type of cement, type of aggregates, water/cement ratio, etc. affects the creep and shrinkage of concrete. The following are several of the predictions methods taken into consideration by the authors of this paper:

- Effective modulus method (McMillan, 1916)
- Age-adjusted effective modulus method (Trost, 1967)
- Double power law for creep (Bazant and Osman, 1976)
- ACI 209 codal provisions (ACI, 1982)
- Double power logarithmic law for creep (Bazant and Chern, 1984)
- CEB-FIP model code 1990 (CEB-FIP, 1990)
- B3 model (RILEM, 1995)
- Muller model; and
- GL2000 model (Gardner and Lockman, 2001a,b).

Early mathematical models were developed with a view to facilitate structural analysis. But computers make it possible to use any kind of model, and thus the recent modeling could focus on experimental data as closely as possible. Effective modulus method, age adjusted effective method, double power law, double power logarithmic law were used by the researchers when very limited experimental data were available, creep and shrinkage was not properly understood and computers were not available for computations. Hence, these models are generally not used for important structures like bridges, nuclear structures, etc. The ACI-209-82 model, the CEB-FIP model code 1990, the B3 model, the Muller model, and the GL2000 model are recent and are based on extensive research as well as experimental studies.

Parameters required for the prediction of creep and shrinkage strains in concrete by these five analytical models are tabulated in Table 2.1. From Table 2.1 it is observed that the GL2000 model, the CEB-FIP model code 1990, and the Muller model requires minimum parameters for the prediction of creep and shrinkage strains in the concrete. To compare the various prediction models, results obtained by these models are to be compared with the experimental results. For this purpose, the experimental results of Russell and Larson (Russell and Larson, 1989) and the RILEM data bank have been selected.

Experimental study of Russell and Larson (Russell and Larson, 1989) was conducted in the Water Tower place, Chicago, a 262-m-high RC building, was instrumented to measure the time-dependent vertical deformations of the columns, walls, and caissons.

Table 2.1 Parameters required by various analytical models for prediction of creep and shrinkage in concrete (Goel, Kumar, and Paul, 2007)

Sl number	Parameter	ACI-209R 82 model	B3 model	CEB-FIP model code 1990/Muller model	GL2000 model
1	Concrete strength at 28 days	✓	✓	✓	✓
2	Modulus of elasticity at the time of loading	✓	✓	×	✓
3	Type of cement	✓	✓	✓	✓
4	Type of curing	✓	✓	×	×
5	Relative humidity	✓	✓	✓	✓
6	Age of concrete at loading	✓	✓	✓	✓
7	Age of concrete at curing	✓	✓	✓	✓
8	Volume-surface ratio	✓	✓	×	✓
9	Cement content	✓	✓	×	×
10	Slump	✓	×	×	×
11	Percentage of fine aggregates by weight	✓	×	×	×
12	Percentage of air content by volume	✓	×	×	×
13	Concrete density	✓	×	×	×
14	Shape of cross section	×	✓	×	×
15	Water content	×	✓	×	×
16	Water-cement ratio	×	✓	×	×
17	Aggregate-cement ratio	×	✓	×	×
18	Cross-sectional area	×	×	✓	×
19	Parameter of the section in contact with atmosphere	×	×	✓	×

This structure was made using Type III cement, normal weight concrete and moist cured for 7 days. The 28-day compressive strength of the concrete varied from 63.0 to 32.45 MPa. Test cylinders were cast and stored in an atmosphere of 23° C and 5% relative humidity. Russell and Larson (1989) reported the long term deformations, creep and shrinkage of this structure.

Based on the results from the study, the following conclusions were given by the authors:

1. The ACI-209 codal provisions are applicable to concretes (using both moist and steam curing; and Types I and III cement) under standard conditions. The standard conditions do not include the concrete strength but its composition, e.g., slump 70 mm, air-content up to 6%, fine aggregates 50%, cement between 279 and 446 kg/m3, curing humidity more than 95%, 40%, etc. Correction factors are applied for the conditions other than standard conditions. The B3 model is applicable to the concretes, having an f_{cm} between 17 and 70 MPa, w/c ratio 0.30–0.85, a/c ratio 2.5–13.5, and cement content (c) 160–720 kg/m3.

The CEB-FIP model code 1990 is applicable to concretes, having an f_{cm} varying from 12 to 80 MPa, h 40–100%, and means temperature 5–30°C. The Muller model is applicable to normal weight plain structural concretes, having an average compressive strength varying from 15 to 120 MPa; moist cured at normal temperature not longer than 14 days, h 40–100%, mean temperature 10–30°C and age at loading at least one day. The GL2000 model is applicable to concretes, having characteristics strength less than 70 MPa and w/c ratios between 0.40 and 0.60.

2. Predictions of creep and shrinkage by the GL2000 model are closest to the experimental results in comparison with other models namely the ACI-209 codal provisions, the B3 model, the CEB-FIP model code 1990, and the Muller model.
3. In the GL2000 model, the number of parameters used to predict creep and shrinkage are also minimal in comparison with the other prediction models and these parameters are readily available. In view of the GL2000 model's simplicity and comparable accuracy with the experimental results, it is concluded that the GL2000 model performs best for shrinkage and creep predictions in the concrete.

2.5 Realistic Long Term Prediction of Prestress Forces in PSC Box Girder Bridges

Creep and shrinkage in concrete are concrete properties very difficult to model, because of the innumerous uncertainties with respect to the concrete materials behaviors

as well as the model uncertainties. The study on the uncertainties in creep and shrinkage effects has been continuously an area of significant efforts (Madsen and Bazant 1983; Bazant and Liu 1985; Bazant 1988; Li and Melchers 1992; Tsubaki 1993; Bazant and Bawaja 1995; Teply, Kersner, and Novak, 1996). Recently, the sensitivity analysis of time-dependent behavior in prestressed concrete (PSC) box girder bridges has been studied (Oh and Yang, 2000).

Creep and shrinkage time-dependant effects on PSC box-girder bridges have not been controlled reasonably regardless of great advances in research in this matter. While other structural behaviors of concrete have been successfully modeled, it is still very cumbersome to fully model the creep and shrinkage.

The finite-element analysis method used in this study is based on the procedure developed originally by Ketchum (1986) and Kang (1989) and improved by Oh and Lee (1996) for the analysis of segmentally erected PSC bridges. This procedure involves an estimation of time-dependent prestress losses in such members and the time-dependent prediction of the accompanying variation in stresses and deformations. A box girder of random plane geometry and variable cross section can be modeled as an assembly of finite elements interconnected at nodal points.

The analytical model consists as described by the authors consists of: 20 nodes, 19 frame elements, and 22 prestressing tendons. The 20 nodes are located at segment joints along the centroidal axis of the box girder. The 19 frame elements are used to model the box girder. Each cantilever segment and each midspan closure segment (key segment) are modeled with one frame element. Eighteen prestressing tendons are used to model the cantilever tendons and four prestressing tendons to model the continuity

prestressing tendons. A portion of the design dead load, equal to 29.4 kN/m, is assumed to be applied permanently, contributing to creep.

In the present study for PSC box girder bridges, the Bayesian updating is applied to the long-term prediction of prestress forces. This method can be applied to the prediction of another long-term creep and shrinkage effect such as deflection or axial shortening of box girders. The present method makes it possible not only to make statistical predictions on the basis of the prior statistical information, but also to update the predictions on the basis of in situ measurement made during construction stages. If the predicted value is outside the specified limit, then a control action may be taken. By the present method one can forecast the time of exceeding the specified limit value during the lifetime of the bridge. Therefore, if a control action for maintenance management of the bridge is to be taken when long-term effects such as prestress forces are outside the control limit, the method developed in this study can be efficiently used. The setting of a control limit and the selection of an optimum method of control alternatives, if needed, are however beyond the scope of this study.

2.6 Cracking Tendency and Drying Shrinkage of Silica Fume Concrete for Bridge Deck Applications

In this paper (Whiting, Detwiler, and Lagergren, 2000) are presented the results of a study intended to evaluate the drying shrinkage of concretes used for full-depth and overlay of highway bridge decks, containing silica fume. The different mixes in this study were prepared with various contents of silica fume and over a range of water to cementitious materials ratios. Concrete samples were tested in the lab using both

restrained and unrestrained drying shrinkage scenarios. Regression analyses were performed on data developed from the laboratory testing and response surface models and analyses of variance were carried out.

Type I/II and type K cement was used in this research. In addition, dry densified silica fume was used. The proportions of the materials used for the concrete mix are listed in Table 2.2. In order to stay consistent with the AASHTO Specifications, the authors maintained a cementitious material content of around 370 kg/m^3. The w/cm ratio varied from 0.35 to 0.45.

In this study the drying shrinkage was measured according to AASHTO T 160, "Length Change of Hardened Hydraulic Cement Mortar and Concrete," the testing specimens were stored at 23 ±1.7 C, 50 ±4% relative humidity. The curing periods were selected to simulate typical good practice for these two types of construction. The lengths were measured at 4, 7, 14, and 28 days, and 8, 16, 44, and 64 weeks. 75 x 75 x 285 mm (gage length of 250 mm) specimens were prepared for every mixture.

For this research the methodology for assessing the cracking tendency, consisted of a method utilized under NCHRP Project 12-37, in which early cracking of full-depth concrete bridge decks was investigated. This methodology consisted in molding a 75 mm thick, 150 mm high ring of concrete around the outside of a steel cylinder with an outside diameter of 300 mm and 19 mm thick walls. This geometry provides restraint against shrinkage while still producing measurable strains from 0 to -1×10^{-4} mm/mm. The inside of the steel ring was instrumented with four strain gages placed at the quarter points around the ring, which were recorded every 30 min by a data acquisition system.

Table 2.2 Mixture proportions of concretes for full-depth bridge decks

Material	Quantities, kg/m^3								
% silica fume	0.0	1.8		6.0			10.2		12.0
w/cm	0.40	0.36	0.43	0.35	0.40	0.45	0.36	0.43	0.40
Cement	369	364	360	343	342	341	331	328	321
Silica fume	0	7	7	22	22	21	37	37	44
Fine aggregate	733	751	716	743	722	699	742	708	720
Coarse aggregate	1071	1097	1046	1085	1055	1020	1084	1034	1052
Water	148	133	158	128	146	163	132	157	146

Fresh concrete was placed into the annular space between the steel ring and an outer sheet metal form in three equal layers, each of which was consolidated by a combination of rodding and external vibration using a small hand-held vibrator.

The concrete was finished at a level approximately 6 mm below the top surface of the mold using a specially designed trowel that conformed to the inside surface of the form. This created a reservoir on top of the concrete into which a saturated limewater solution was placed. The entire mold was then covered with polyethylene sheeting. After the specified period of moist curing, the limewater was removed and the exterior form stripped from the specimen. The top surface of the concrete was then covered with a polyethylene sheet affixed to the concrete with silicone sealant. Drying then occurred from the exposed sides of the concrete specimen. This technique allowed for easy detection of cracking, as when a crack suddenly reduced the stress locally, and resulted in a local decrease in strain, which was monitored by the strain gage.

This research showed that the additional cracking tendency of concrete containing silica fume is present only when poor curing conditions are used. Concrete cured properly in a moist environment for 7 days, no relevant evidence of early-age cracking was present in concretes with silica fume. When comparing the long term shrinkage of concretes with silica fume no significant cracking pattern difference was found when compared to

concretes without silica fume. The researchers recommend that concrete with silica fume, should be carefully cured in a moist ambient for 7 days.

Finally the authors concluded that the cracking is highly influenced by the amount of cement contained in the concrete mixture. Concrete mixes with high cementituos materials content, tends to have greater shrinkage because of the higher paste content. The modern practice consists of increasing the aggregates proportions in the concrete mixes in order to reduce de cement paste proportion, therefore reducing the shrinkage potential.

CHAPTER 3

TEST DESCRIPTION AND RESULTS

Concrete tests are often specified with the purpose of having a strict quality control and to assure compliance with the contract documents specifications. In other cases, like ours, tests are prescribed in order to characterize the concrete subject to research. Thus, it can be comparable to the results of future or past research. In addition, if the results of different research projects are to be compared, the tests on what those research are based should be performed following certain standards and procedures.

In order to characterize the mechanical and durability properties of the concrete used for this research, five different tests were selected. The tests and the ASTM standard to which they conform are summarized in Table 3.1.

A more detailed description of each test in Table 3.1 is presented below.

Table 3.1 Summary of performed tests

Test	ASTM Standard(s)
3.1 Compressive Strength	C 31 & C 39
3.2 Modulus of Elasticity	C 469
3.3 Shrinkage	C 157
3.4 Freeze and Thaw Resistance	C 666
3.5 Chloride Ion Penetration	C 1202

3.1 Compressive Strength

The compressive strength of concrete is the most specified property of concrete; it is the most commonly used design criteria specified by engineers in the design process. Various reasons make the compressive strength the most used property of concrete, one of the primary reasons is, the testing of the compressive strength is fairly easy. In addition research has been conducted to correlate compressive strength to all other major properties of concrete, such as elastic modulus, tensile strength, permeability, and resistance to weather agents.

The compressive strength of concrete is determined by loading the testing specimen to failure. Failure being the state of deformation or cracking such as the material is no longer able to sustain the applied load.

In order to attain a certain level of quality in the concrete mixing, three key aspects must be taken into consideration: selection and proportioning of the materials, curing conditions, and tests specifications.

3.1.1 Selection and proportioning of the materials

Since concrete is the product of mixing different materials, the interaction of these materials influence the compressive strength of concrete. Consequently the selection and proportioning of the materials is critical. In the following paragraphs, the most common materials and their importance in the compressive strength of concrete is presented.

3.1.1.1 Cement type. The material that has most influence on the concrete properties, with respect to the other components, is the cement. As much as it is in quality, as it is in quantity. Neville (1996) describes the Portland cement as a cement

obtained by intimately mixing together calcareous and argillaceous, or other silica, alumina, and iron oxide-bearing materials, burning them at a clinkering temperature, and grinding the resulting clinker.

The ASTM standard specification for Portland cement (ASTM C150) classifies the Portland cement into eight different types, manufactured to meet different chemical and physical requirements for specific purposes. The classification of the Portland cement given by the ASTM 150 is presented in Table 3.2.

The relationship between the cement type and the compressive strength of the concrete is showed in Figure 3.1.

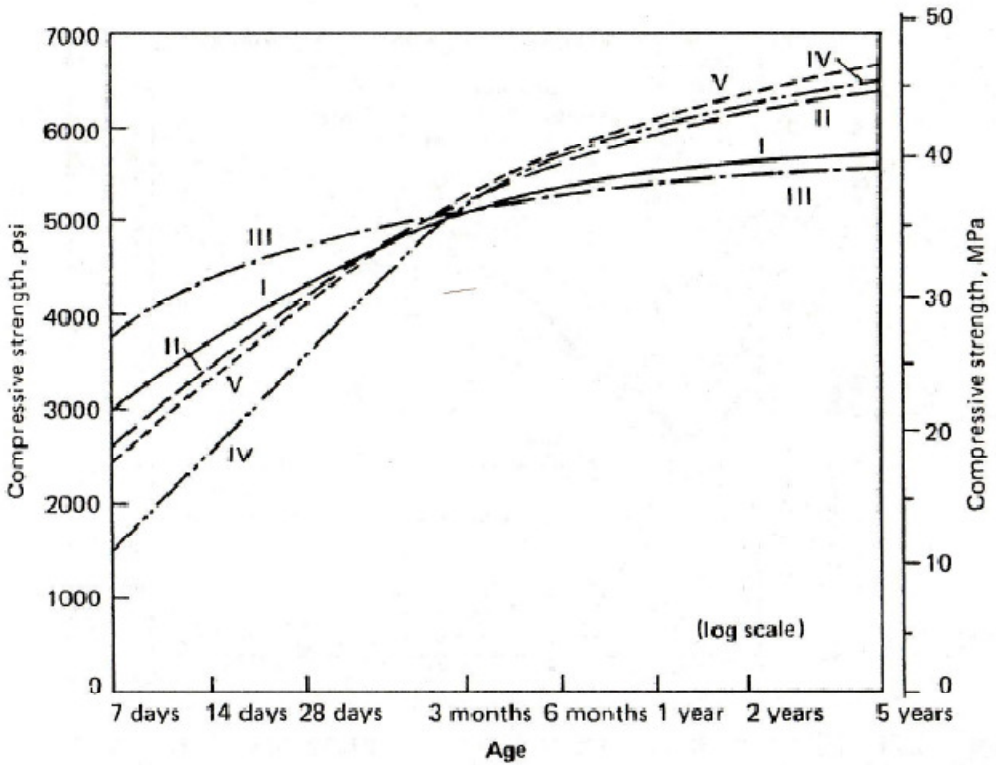

Figure 3.1 Effects of type of cement on compressive strength of concrete (US Bureau of Reclamation, 1966).

Table 3.2 Classification of portland cement (ASTM 150)

Type	Use
I	When the special properties specified for any other type are not required
I A	Air-entraining cement for the same uses as Type I, where air-entrainment is desired
II	For general use, more specially where moderate sulfate resistance or moderate heat of hydration is desired.
II A	Air-entraining cement for the same uses as Type II, where air-entrainment is desired
III	For use when high early strength is desired
III A	Air-entraining cement for the same uses as Type III, where air-entrainment is desired
IV	For use when a low heat of hydration is desired
v	For use when high sulfate resistance is desired

When selecting the type of cement one particular property that affects the hydration of cement apart from its chemical composition, is the fineness of the cement ground. The finer the cement is ground, a direct increase in the hydration heat will occur, which results in early high strengths gains. A typical graph relating the cement fineness and the concrete strength at different ages is depicted in Figure 3.2.

3.1.1.2 Water/cement ratio. The water cement ratio of any concrete mix should be selected considering two main factors, strength and workability. It has been vastly shown that the strength of concrete is conversely proportional to the water cement ratio. Therefore a lower w/c ratio results in a higher concrete strength. On the other hand, concrete mixes with too low of a w/c ratio lack of workability. Therefore, balance should be met between strength and workability.

3.1.1.3 Aggregates. Since the aggregates occupy more than 60% of the concrete volume and are the strongest individual component, its properties influence the final compressive strength of the concrete. The fineness modulus and the maximum size of aggregate affects the fine to coarse aggregate proportion, as well as the water and cement quantities. Aggregate type also affects workability, economy and shrinkage tendencies.

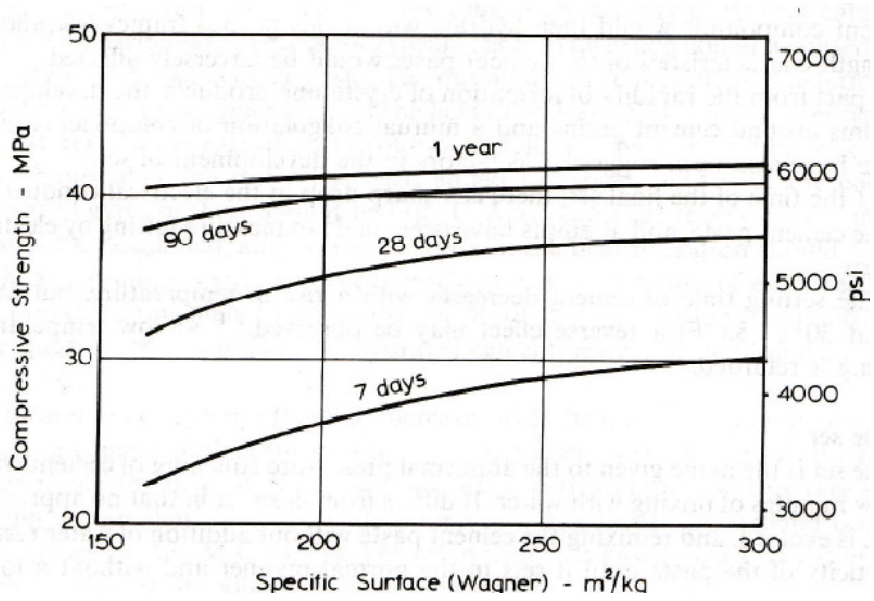

Figure 3.2 Relationship between fineness of cement and concrete strength at different ages (Neville,1996).

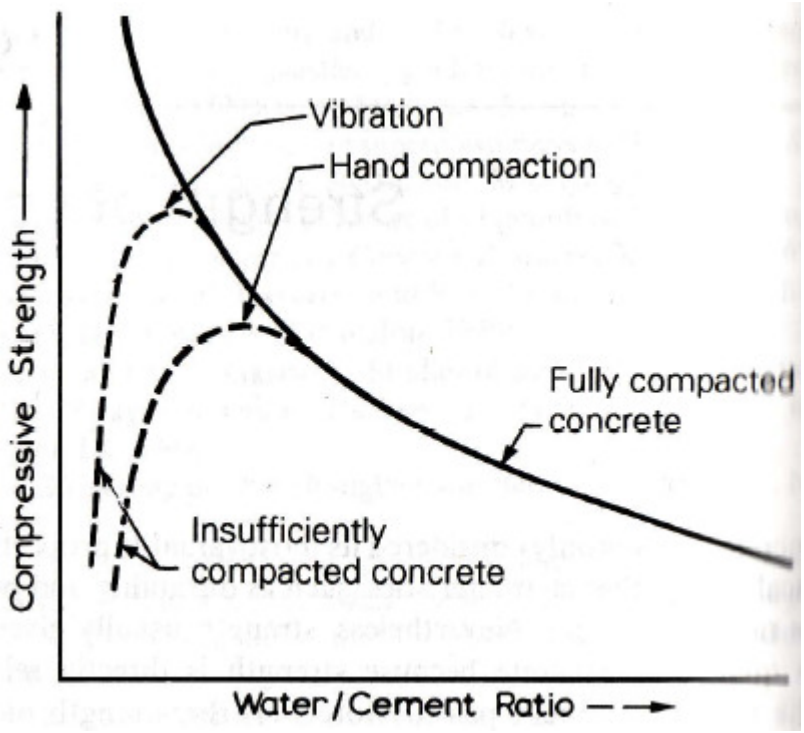

Figure 3.3 The relation between strength and the water/cement ratio of concrete (Neville, 1996).

3.1.1.4 Admixtures. The concrete properties can be enhanced by the inclusion of admixtures. There are several types of admixtures, among them: water reducers, air entrainers, setting time retardants, etc. The most commonly used admixture to increase the compressive strength is the water reducer or superplasticizer, because they allow, for a given workability, less use of water, which traduces to a higher strength.

The proportions of materials for the concrete mixes used for the scope of this research are listed in Table 3.3. For proprietary reasons, the mix design used in the Eagle Precast sample cannot be published in this research.

3.1.2 Curing conditions

Since the concrete bleeds the excess water, and this water is evaporated due to the climate conditions, a humid environment should be provided to enhance the curing process.

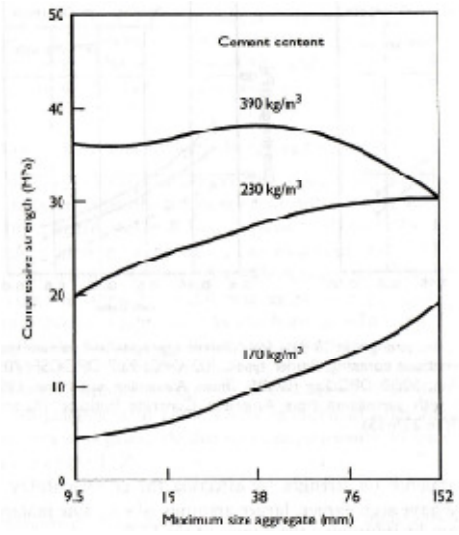

Figure 3.4 28-day compressive strength of concrete as influenced by maximum size of aggregate and cement content (Higginson, 1966).

The proper concrete curing should start once the initial setting of the concrete has occurred, and common practice recommends that concrete should be cured for not less than seven days.The time of curing is directly proportional to the final strength of concrete; the longer the curing period, the higher the final strength of concrete.

3.1.3 Test specifications

All the compressive strength testing done for the scope of this research was made according the provisions of the ASTM C39 Standard.

Table 3.3 Mix designs

Materials	669 Bridge Deck	668 Bridge Deck
Cement (lbs/yd^3)	556	489
Fly Ash (lbs/yd^3)	103	122
Fine Aggregate (lbs/yd^3)	1604	1204
Coarse Aggregate (lbs/yd^3)	1355	1718
water (lbs/yd^3)	270	243
w/cm	0.41	0.40

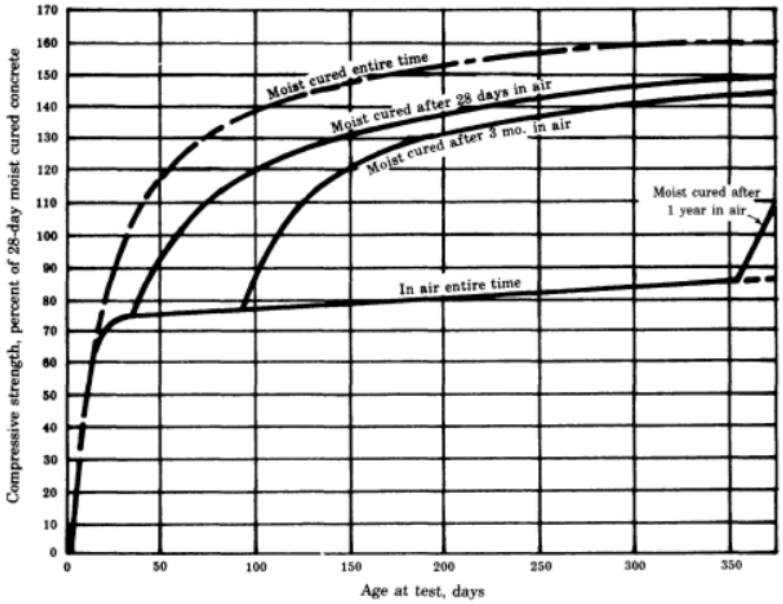

Figure 3.5 Effects of moist curing on the strength of concrete (Portland Cement Association).

The sampling of the concrete used in these tests conforms to the ASTM C31 Standard.The most common specimen used for the compressive strength testing was the 4-by-8 in. (diameter by height) cylinder.

For this project, the test cylinders were cast at the time each of the decks were poured. For the compressive strength test, 4-by-8 in. cylinders were cast. Proper curing conditions were provided for the testing cylinders. The standard ages for testing the compressive strength of concrete are: 1, 3, 7, 14, 28, and 56 days. Two cylinders were tested on each of testing days. The two cylinders were average to obtain the measured compressive strength. In order to calculate the compressive strength of the concrete Eq. 3.1 was used.

$$\sigma = \frac{P}{A} \tag{3.1}$$

where

σ = the compressive strength at the age of testing (psi).

P= Failure load (lbs).

A= Cross-sectional area of the concrete specimen (in^2). The cross-sectional area of a 4-by-8 in. cylinder is calculated to be 12.57 in^2.

The compressive strength tests results for the Eagle Precast Samples, the 669 Bridge Deck and the 668 Bridge Deck, are presented in Table 3.4, Table 3.5, and Table 3.6, respectively.

Table 3.4 Eagle precast compressive strength test results

Days after Casting	Cylinder	Load (lb.)	σ (psi)	Avg.σ (psi)
1	4 x 8 (1)	77169	6141	6048
1	4 x 8 (2)	74825	5954	
3	4 x 8 (3)	105223	8373	9666
3	4 x 8 (4)	137702	10958	
7	4 x 8 (5)	122474	9746	9945
7	4 x 8 (6)	127473	10144	
14	4 x 8 (9)	138246	11001	11043
14	4 x 8 (10)	139284	11084	
28	4 x 8 (11)	151423	12050	12280
28	4 x 8 (12)	157200	12510	
56	4 x 8 (13)	161375	12842	12698
56	4 x 8 (14)	157762	12554	

Table 3.5 669 Bridge deck compressive strength test results

Days after Casting	Cylinder	Load (lb.)	σ (psi)	Avg.σ (psi)
1	4 x 8 (1)	22712	1807	1834
1	4 x 8 (2)	23373	1860	
3	4 x 8 (3)	41576	3309	3162
3	4 x 8 (4)	37883	3015	
7	4 x 8 (5)	49790	3962	3960
7	4 x 8 (6)	49724	3957	
14	4 x 8 (9)	61922	4928	4828
14	4 x 8 (10)	59412	4728	
28	4 x 8 (11)	70006	5571	5796
28	4 x 8 (12)	75657	6021	
56	4 x 8 (13)	80580	6412	6388
56	4 x 8 (14)	79980	6365	

Table 3.6 668 Bridge deck compressive strength test results

Days after Casting	Cylinder	Load (lb.)	σ (psi)	Avg.σ (psi)
11	4 x 8 (1)	57564	4581	4777
11	4 x 8 (2)	62496	4973	
19	4 x 8 (3)	69032	5493	5399
19	4 x 8 (4)	66655	5304	
28	4 x 8 (5)	75181	5983	5973
28	4 x 8 (6)	74948	5964	
56	4 x 8 (9)	85648	6816	6597
56	4 x 8 (10)	80158	6379	

It is shown in Tables 3.4 through 3.6, that the respective 28 compressive strengths (f'_c) for the Eagle Precast, 669 Bridge Deck, and 668 Bridge Deck were 12,280 psi, 5,796 psi, and 5,973 psi. It is important to mention that the Eagle Precast sample corresponds to the Self Consolidated High Performance Concrete used in the casting of the precast bridge decks. Each of the mix designs exceeded to required compressive stress of 4,000 psi according to the UDOT Bridge deck standards.

Figure 3.6 shows a plot of the compressive strength versus time for all three concrete samples.

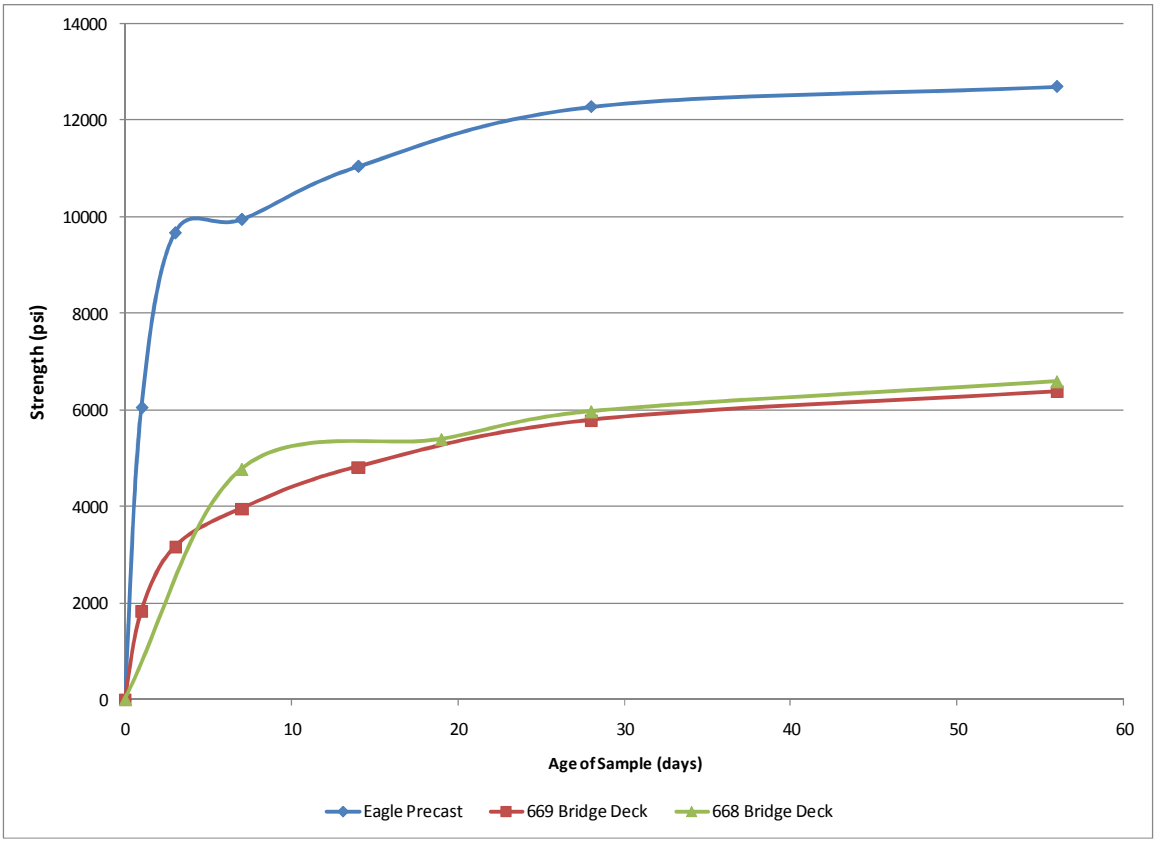

Figure 3.6 Compressive strength vs. time for all three concrete samples.

3.2 Modulus of Elasticity

When the concrete is loaded within its elastic region, it is assumed that the stress is directly proportional to the strain. Taking advantage of this property, a concrete specimen can be axially loaded, and the shortening of the cylinder in the direction of the load is measured. Knowing the cross-sectional area of the cylinder and the length of the gauge, measuring the deformation the stress and strain can be calculated and then plotted on a curve. The slope of that curve in the elastic region is a measure of the modulus of elasticity.

For this research the procedures followed to perform the modulus of elasticity test were those contained in the ASTM C469 Standard. The concrete sample used for these tests consisted in 6-by-12 in. cylinders.

When conducting a modulus of elasticity test, two aspects must be taken into consideration: 1) the loading speed and 2) the maximum load applied.

For the first aspect, the ASTM standard states that the rate of loading is to be in the range of 35 ± 5 psi/s (in our case 59,000 lbs/min), and this loading rate must remain constant throughout the duration of the test. The reason for having a loading range is because at slower rates of loading additional creep can be developed in the specimen. This creep effect can be reduced by a more rapid rate of loading. For the second aspect, the ASTM procedure mandates that the maximum load applied to the specimen shall not exceed 40 percent of the tested ultimate load. The justification for this limit is due to micro cracks that develops at higher loads and propagates throughout the specimen negatively affecting the curvature of the stress-strain curve.

Two 6-by-12 in. specimens were tested at the ages of: 1, 3, 7, 14, 28, and 56 days. For each day, an average modulus of elasticity was calculated for each set of samples. The testing procedure was as follows: first a 4-by-8 in. cylinder was tested in order to determine the ultimate compressive strength of the concrete sample. Second, the 6-by-12 in. cylinders were loaded to the equivalent load that produces 40 percent of the ultimate strength. During the test the deflections were monitored with an electronic LVDT. The loading was registered in the data acquisition system and use to calculate the modulus of elasticity using the Eq. 3.2.

$$E = \frac{\sigma_2 - \sigma_1}{\varepsilon_2 - 0.000050} \tag{3.2}$$

where

E= Chord or Secant Modulus of Elasticity (psi).

σ_2= Stress at 40 percent of the failure load (psi).

σ_1= Stress at a longitudinal strain of 0.000050.

ε_2= Strain corresponding to stress σ_2.

The results of the modulus of elasticity tests performed to the Eagle Precast concrete samples are shown in Table 3.7. The results of the modulus of elasticity tests performed to the 669 Bridge Deck concrete are shown in Table 3.8. The results of the modulus of elasticity tests performed to the 668 Bridge Deck concrete are shown in Table 3.9.

Table 3.7 Eagle precast sample modulus of elasticity

Test Age (d)	Average E (psi)
1	3.318E+06
3	4.017E+06
7	4.460E+06
14	4.991E+06
28	4.815E+06
56	5.074E+06

Table 3.8 669 Bridge deck sample modulus of elasticity

Test Age (d)	Average E (psi)
1	2.580E+06
3	3.191E+06
7	3.751E+06
14	3.872E+06
28	4.389E+06

Table 3.9 668 Bridge deck sample modulus of elasticity

Test Age (d)	Average E (psi)
11	4.210E+06
18	4.117E+06
28	4.407E+06
60	4.447E+06

A plot of modulus of elasticity vs. time is depicted in Figure 3.7. As expected the modulus of elasticity reduces its rate of increasing after 28 days. The higher modulus of elasticity was observed in the concrete of the Eagle Precast sample, with a modulus of elasticity of 4,815 ksi, this was expected, since the modulus of elasticity is dependent on the concrete strength, and this is the concrete with the highest specified strength.

Figure 3.8 shows a plot of the modulus of elasticity calculated using the Eq. 3.3 given by the ACI 318 §8.5.1 and the measured values of average σ (psi) on Tables 3.3, 3.4, and 3.5 for the different concrete samples.

$$E = 57{,}000\sqrt{f'c} \qquad (3.3)$$

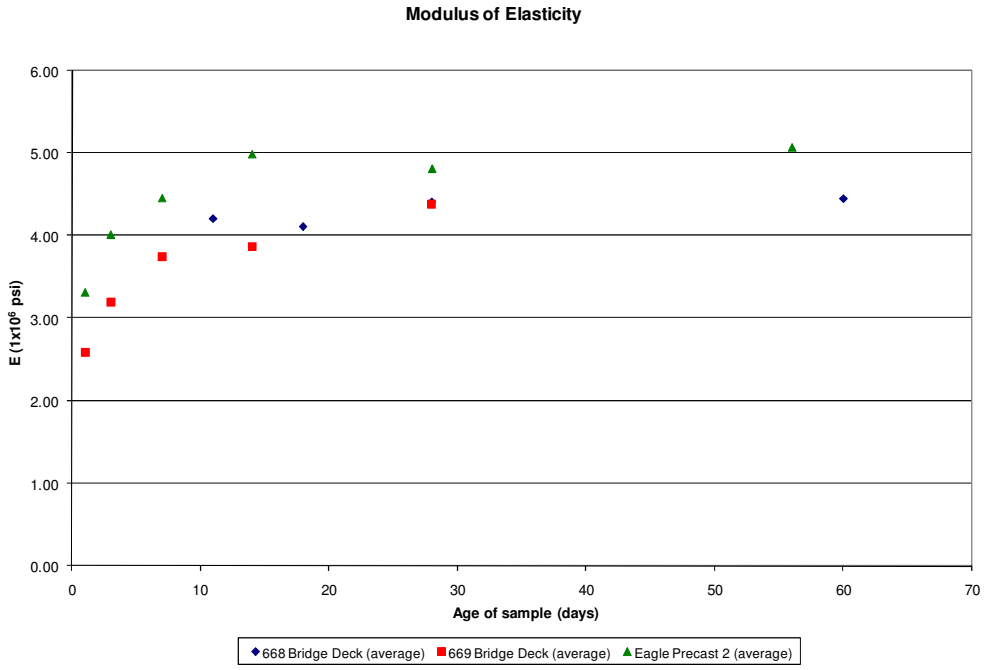

Figure 3.7 Summary of the modulus of elasticity vs. time for all three samples.

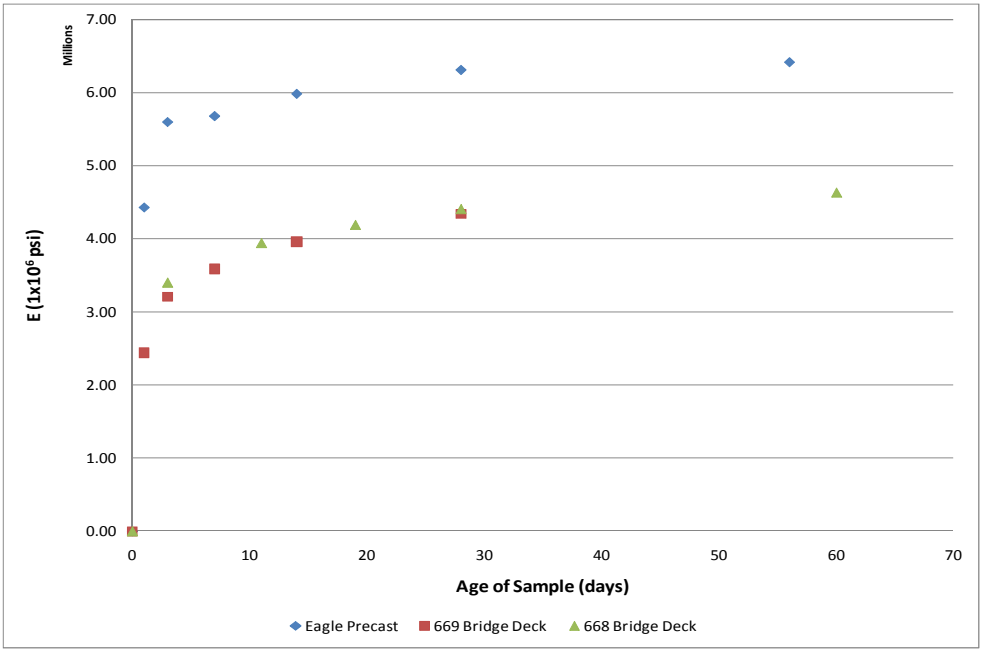

Figure 3.8 Modulus of elasticity vs. time using the Eq. 3.3.

It can be observed that the Eq. 3.3 overestimates the values of modulus of elasticity for the higher strength concrete (Eagle Precast) with a ratio of the calculated over the measured of 1.31 at 28 days of age. For the samples pertaining to the 669 Bridge Deck and 668 Bridge Deck, the Eq. 3.3 gives a very accurate results with a ratio of the calculated over the measured of 0.98, and 0.99, respectively at 28 days of age.

3.3 Shrinkage

Since the concrete is a porous solid, it shares a property common to most porous solids in that it shrinks as a result of a reduction of its water content. Since the most common use of concrete is in the making of reinforced concrete structures, the restraint imposed to the concrete by the inclusion of reinforcing steel causes induced stresses to develop in the structure. If these stresses are higher than the tensile strength of concrete, cracks will form, compromising the structural integrity of the structure.

The shrinkage of the concrete is influenced by the elastic properties of the cement paste and aggregates and their shrinkage. In addition to the influence of the restrain imposed by the aggregates and the unhydrated cement, the relative humidity of the environment, drying time and water cement ratio also influence the magnitude of the shrinkage. Because shrinkage is affected by so many different factors, accurate predictions are difficult to determine.

The shrinkage tests performed on the concrete deck samples for this research were made following the provisions in the ASTM C157 standard. The test specimens consisted of concrete prisms with dimensions equal to 3-by-3-by-16 in. Metal studs where embedded at both ends of the specimen, in order to fit the reading apparatus. The

specimens where kept out of the moisture room, in order to simulate field curing conditions.

An electronic gage comparator system was used to take readings at the ages of: 3, 7, 14, 28, and 56 days.

Shrinkage strain at each test day was calculated using the Eq. 3.4.

$$\varepsilon = \frac{\text{CR - IR}}{\text{G}} \tag{3.4}$$

where

ε= strain of the specimen at test age.

CR= Comparator reading at the test age.

IR= Initial reading.

G= Gage length.

Table 3.10 shows the raw tests measurements for all three concrete deck samples. Using Eq. 3.3 and the raw data in Table 3.10 the strain was calculated. The results are shown in Table 3.11, Table 3.12, and Table 3.13. A plot of the strain of all three samples vs. time is shown in Figure 3.9.

Table 3.10 Shrinkage test recordings

age (days)	Eagle Precast Samples			age (days)	669 Bridge Deck Samples			age (days)	668 Bridge Deck Samples	
	1	2	3		1	2	3		1	2
original	0.3880	0.3735	0.2594	original	0.3176	0.2824	0.2555	original	0.2017	0.1314
3	0.3872	0.3727	0.2583	3	0.3159	0.2806	0.2537	11	0.1974	0.1271
7	0.3866	0.3712	0.2552	7	0.3123	0.2780	0.2513	18	0.1974	0.1270
14	0.3822	0.3686	0.2537	14	0.3101	0.2764	0.2473	28	0.1963	0.1262
28	0.3804	0.3667	0.2511	28	0.3091	0.2754	0.2458	60	0.1950	0.1246
56	0.3798	0.3658	0.2502	56	N/A	N/A	N/A		N/A	N/A

Table 3.11 Strain of eagle precast samples in με

age (days)	Eagle Precast Samples			Average
	1	2	3	
1	0.0	0.0	0.0	0.0
7	162.3	214.5	324.6	233.8
14	220.3	268.1	314.5	267.6
28	353.6	307.2	394.2	351.7
56	394.2	365.2	452.2	403.9

Table 3.12 Strain of 669 Bridge deck samples in με

age (days)	669 Bridge Deck Samples			Average
	1	2	3	
1	0.0	0.0	0.0	0.0
7	272.5	220.3	208.7	233.8
14	440.6	353.6	481.2	425.1
28	539.1	452.2	608.7	533.3

Table 3.13 Strain of 668 Bridge deck samples in με

age (days)	668 Bridge Deck Samples		Average
	1	2	
1	0.0	0.0	0.0
19	249.3	255.1	252.2
28	313.0	301.4	307.2
60	388.4	394.2	391.3

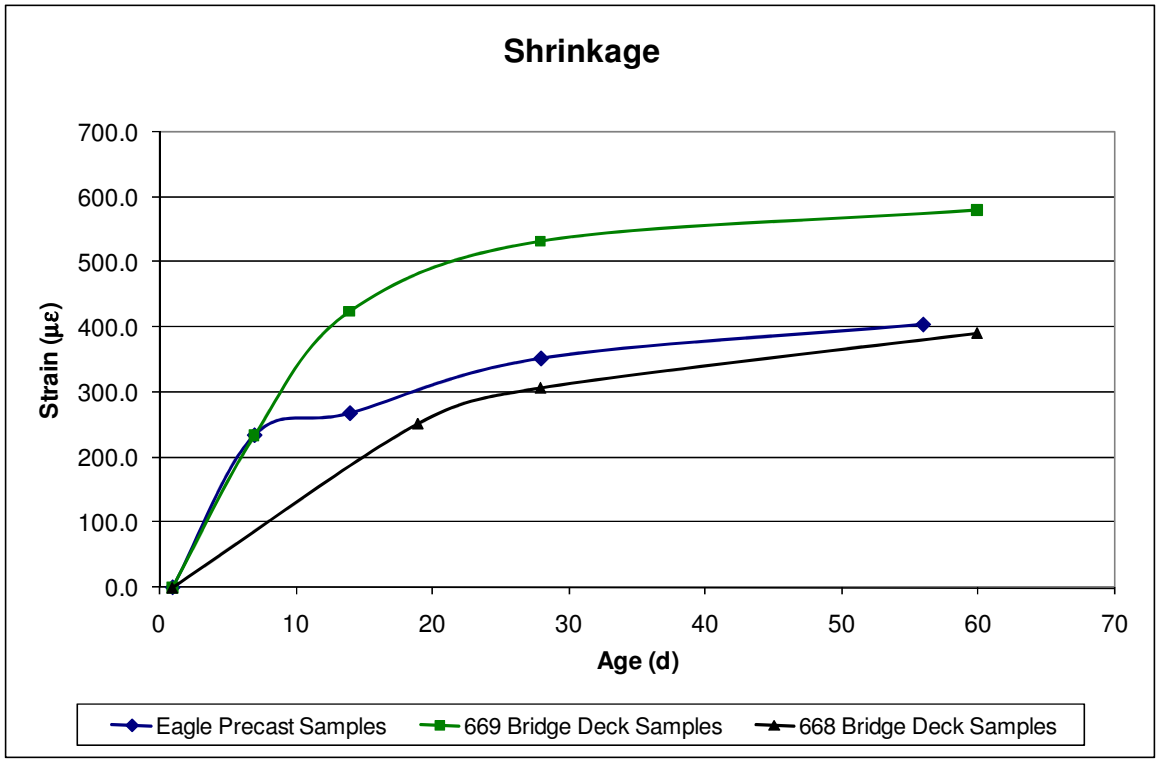

Figure 3.9 Strain vs. time.

3.4 Freeze and Thaw

Most concrete decks are exposed to climate changes. When the structure is subjected to some degree of saturation, a problem arises; this problem is the freezing of the water entrained in the concrete. Since water increases in volume by approximately 9%, this expansion translates in pressurizing the water in the concrete pores, and if this pressure exceeds the concrete capacity in tension, a crack will form. In addition, concrete subjected to repeated cycles of freezing and thawing deteriorates over time.

This problem is aggravated when thawing occurs. Thawed water migrates to other parts of the structure, resulting in different cracks. When the structure is subjected to

various cycles of freezing and thawing different parts of the structure begin to crack. In the beginning this could express as surface scaling, but in advanced stages this could become in permanent damage to the concrete deck.

The resistance of the concrete to these freeze-thaw cycles is dependant of many factors, such as the strength of the hardened cement paste, air entrained in the concrete and its porosity. A concrete with a low water to cement ratio will be less likely to be affected by the freeze and thaw cycles, due to its relatively low porosity.

In order to simulate this freeze-thaw condition in the lab, 3-by-3-by-16 in. samples of concrete were made (Figure 3.11) from each of the deck concretes. The procedure followed to perform this test was the one described in the ASTM C666 Standard, Procedure A. The test specimens were placed in a freeze/thaw chamber submerged in water (Figure 3.10), the water above the surface of the test specimens could not be lower than 1/32" and could not surpass 1/8". The test specimens remained in the freeze-thaw chamber for approximately 300 cycles. Every 30 cycles the test was stopped, and then the fundamental transverse natural frequency of the test specimen was measured using a dynamic signal analyzer (Figure 3.12).

With these values of fundamental natural frequency, the Relative Dynamic Modulus of Elasticity can be calculated using Eq.3.5.

$$\boldsymbol{P_C = \frac{n_1^2}{n^2} \times 100} \qquad (3.5)$$

where

P_c = Relative dynamic modulus of elasticity.

n_1 = Fundamental transverse natural frequency of the sample at time of testing.

Figure 3.10 Freeze thaw chamber.

Figure 3.11 Concrete samples for the freeze-thaw test.

Figure 3.12 Dynamic signal analyzer.

n= Fundamental transverse natural frequency of the sample at the initial time.

The values of the fundamental transverse natural frequency collected from each of the deck samples are listed in the Table 3.14, it can be seen that no data could be acquired from the Eagle Precast sample 3 due to excessive deterioration of the sample as can be seen in Figure 3.13.

Table 3.14 Fundamental transverse natural frequencies

No. Cycles	Frecuency (KHz)							
	Eagle Precast 2			669 Bridge Deck			668 Bridge Deck	
	Sample 1	Sample 2	Sample 3	Sample 1	Sample 2	Sample 3	Sample 1	Sample 3
0	4.82	4.90	4.64	4.82	4.79	4.78	4.78	4.75
68	4.63	4.74	4.12	4.75	4.83	4.84	4.72	4.76
108	4.67	4.74	N/A	N/A	4.84	N/A	4.92	4.91
138	4.98	5.06	N/A	4.95	5.07	5.07	5.06	5.02
168	4.90	5.05	N/A	4.70	4.85	4.92	5.02	5.01
198	4.89	5.01	N/A	4.85	4.86	4.90	5.05	5.04
228	4.78	5.04	N/A	4.81	4.81	4.98	5.09	5.07
258	4.90	5.05	N/A	4.72	4.87	4.93	5.10	5.06
288	4.88	5.00	N/A	4.88	4.92	4.95	5.13	5.01
318	4.92	5.02	N/A	4.89	4.96	5.01	5.10	5.10

Figure 3.13 Eagle precast sample 3.

Using Eq. 3.5, and the fundamental natural frequencies data contained in Table 3.14, the relative dynamic modulus of elasticity was calculated, the results are in Table 3.15.

Table 3.16 shows the durability factors calculated for every sample. From the results it can be seen that the lowest durability factor for either sample was no lower than 0.96.

3.5Chloride Ion Penetration

The chlorides do not attack the concrete directly; they attack the reinforcing steel, being a major cause of corrosion of the rebar. Once corrosion commences, the rebar expands, subsequently cracking the concrete.

Table 3.15 Relative dynamic modulus of elasticity

No. Cycles	Frecuency (KHz)							
	Eagle Precast 2			669 Bridge Deck			668 Bridge Deck	
	Sample 1	Sample 2	Sample 3	Sample 1	Sample 2	Sample 3	Sample 1	Sample 3
0	100.00	100.00	100.00	100.00	100.00	100.00	100.00	100.00
68	96.16	96.73	88.79	98.55	100.84	101.26	98.64	100.11
108	96.99	96.73	N/A	N/A	4.84	N/A	102.76	103.22
138	103.39	103.31	N/A	102.61	105.76	106.11	105.73	105.58
168	101.77	103.06	N/A	97.51	101.25	102.93	104.96	105.43
198	101.56	102.24	N/A	100.62	101.46	102.51	105.58	105.96
228	99.27	102.86	N/A	99.79	100.42	104.18	106.42	106.59
258	101.77	103.06	N/A	97.93	101.67	103.14	106.61	106.44
288	101.35	102.04	N/A	101.24	102.71	103.56	107.25	105.43
318	102.18	102.45	N/A	101.45	103.55	104.81	106.52	107.32

Table 3.16 Durability factors

No. Cycles	Frecuency (KHz)							
	Eagle Precast 2			669 Bridge Deck			668 Bridge Deck	
	Sample 1	Sample 2	Sample 3	Sample 1	Sample 2	Sample 3	Sample 1	Sample 3
0	1.00	1.00	1.00	1.00	1.00	1.00	1.00	1.00
68	0.96	0.97	0.89	0.99	1.01	1.01	0.99	1.00
108	0.97	0.97	N/A	N/A	1.01	N/A	1.03	1.03
138	1.03	1.03	N/A	1.03	1.06	1.06	1.06	1.06
168	1.02	1.03	N/A	0.98	1.01	1.03	1.05	1.05
198	1.02	1.02	N/A	1.01	1.01	1.03	1.06	1.06
228	0.99	1.03	N/A	1.00	1.00	1.04	1.06	1.07
258	1.02	1.03	N/A	0.98	1.02	1.03	1.07	1.06
288	1.01	1.02	N/A	1.01	1.03	1.04	1.07	1.05
318	1.02	1.02	N/A	1.01	1.04	1.05	1.07	1.07

This is why the study of the chloride ion penetration through the deck concrete cover is important.

The chlorides ions can be present in the concrete from different sources; one of the major causes of the presence of chloride ions in bridge decks is the deicing salt. Other important source of chloride ions is the sea water in contact with concrete structures, airborne sea water drops that travels from the sea shore into the main land. Submerged

structures are subject to a deeper penetration of the chloride ions, but since oxygen is not present in the cathode corrosion of the steel is not a problem.

The procedure followed in this research for investigating the ability of the concrete deck samples to resist the chloride ion penetration is the one described in the ASTM C1202 standard. For this test, two samples of each concrete deck were prepared. The preparation of the samples was as follows: first two slices of two inches in thickness were cut from a 4-by-8 in. concrete cylinder; the concrete was then covered in the side surface by a concrete water sealant, in order to prevent water migrating from the inside.

After that the samples were placed in a vacuum desiccator (Figure 3.15) and the air was removed over a 3-hour period. After which, the specimen was left to soak in distilled water for 18 hours. Subsequently, the specimen was removed from the water, the excess water was blotted off, and the specimen was transferred to the testing apparatus. The contact surface between the specimen and the testing apparatus was sealed with a special silicone sealer.

Figure 3.14 Chloride ion penetration apparatus.

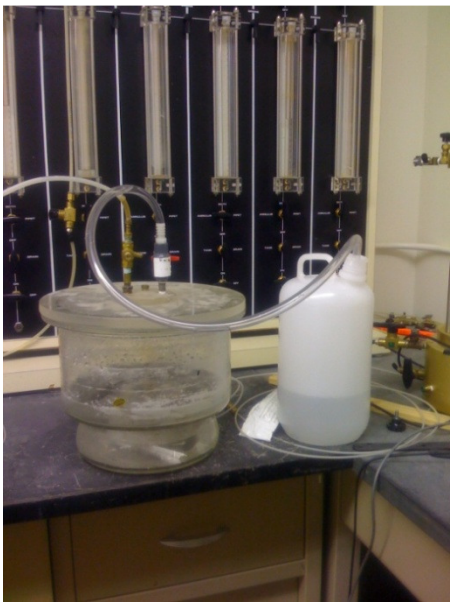

Figure 3.15 Vacuum desiccator apparatus.

Then the cell that is connected to the negative terminal of the power supply was filled with a 3.0% NaCl solution, the other cell (the one that is connected to the positive terminal of the power supply) with a 0.3 N NaOH solution. Connections were made through a voltage power supply. The power was turned on then the voltage was set to 60.0 V ± 0.1 V and the initial current was then registered. For a period of 6 hours, the current was read and recorded every 30 min.

According to the ASTM C1202, the total charge passed through the 2-in. specimen is a measure of the conductance of the concrete during the period of the test. Since the current was recorded every 30 min, the standard recommends the following equation for calculating the charge passed by the specimen:

$$Q = 900(I_0 + 2I_{30} + 2I_{60} \ldots + 2I_{300} + 2I_{330} + I_{360}) \quad (3.6)$$

where

Q = Charge passed (coulombs).

I_o = Current (amperes) immediately after voltage is applied.

I_t = Current (amperes) at t min after voltage is applied.

This test is standardized for specimens with a diameter of 3.75 in. Since our specimens were 4 inches in diameter a correction shall be made according to the ASTM, using the following equation:

$$Q_S = Q\left(\frac{3.75}{X}\right)^2 \quad (3.7)$$

where

Q_s = Charge passed (coulombs) through a 3.75-in. (95-mm) diameter specimen,

Q = Charge passed (coulombs) through x in. diameter specimen.

x = Diameter (in.) of the nonstandard specimen.

Table 3.17 shows the recorded current readings for all of the three samples. Using these recorded readings and with the aid of Eq. 3.6 the charge passed was calculated and the results are given in the Table 3.18.

The ASTM C1202 gives some guidelines for comparing the results obtained in this test. These guidelines are presented in Table 3.19 excerpted for the standard. Judging by the results presented in Table 3.18, and comparing with the guidelines in Table 3.19, all three concretes have very low chloride ion permeability.

Table 3.17 Recorded current readings

Minutes elapsed	Current (miliamp)					
	Eagle Precast		669 Bridge Deck		668 Bridge Deck	
	1	2	1	2	1	2
0	13.6	16.5	37.4	40.0	42.1	38.2
30	11.5	16.3	35.4	40.0	44.3	38.1
60	10.8	15.2	35.1	38.2	46.8	38.0
90	10.3	15.0	34.8	38.1	49.0	37.5
120	10.0	15.0	34.5	37.8	50.3	37.3
150	9.4	14.8	34.5	37.6	51.0	37.2
180	9.1	14.7	33.8	37.5	51.9	37.3
210	8.9	14.5	33.7	37.1	52.3	36.9
240	8.7	14.1	33.6	37.1	53.0	36.8
270	8.6	14.0	33.3	36.5	53.1	36.7
300	8.5	14.0	33.0	36.4	53.3	36.8
330	8.4	13.9	33.0	36.7	53.5	36.3
360	8.2	13.9	33.1	36.4	54.0	36.1

Table 3.18 Charge passed through the specimens (coulombs)

	Eagle Precast	669 Bridge Deck	668 Bridge Deck
Q(coulombs)	262.6	775.0	947.3
Q_s(coulombs)	230.8	681.2	832.6

Table 3.19 Chloride ion permeability based on charged passed

Charge Passed (coulombs)	Chloride Ion Penetrability
>4,000	High
2,000–4,000	Moderate
1,000–2,000	Low
100–1,000	Very Low
<100	Negligible

CHAPTER 4

PREDICTED VS. MEASURED PRESTRESS LOSS AND DEFLECTIONS IN HIGH PERFORMANCE CONCRETE GIRDERS

In this chapter a comparison between measured prestress loss and predicted prestress loss methods is presented and discussed. Prestress losses were monitored in six HPC bridge girders. The bridge instrumented was the 669 State Bridge near Farmington, Utah. These measured losses were compared to predicted losses according to four sources. Prestress loss predictive methods considered for this research were: 1- AASHTO LRFD 2004, 2- AASHTO LRFD 2004 Refined, 3- AASHTO LRFD 2007, and 4- AASHTO LRFD Lump Sum method.

On the second part of this chapter a comparison of measured deflections and predicted deflections of concrete bridge girders are presented. The camber in the SR18/SR516 Bridge in the state of Washington was monitored and the measured camber compared to the following predictive methods: 1- Time dependent method described in NCHRP Report 496, 2- PCI Multiplier Method, and 3- Improved PCI Multiplier method.

4.1 Predicted vs. Measured Prestress Loss

Accurate prediction of the long term prestress losses in concrete-bridge girders is an important part of the design process. An overprediction in the prestress loss could mean a limitation of the span length of the girder, and a considerable increase in the prestressing force required to overcome such losses. On the other hand, an under-prediction of the prestress losses could translate into undesired deflections and cracking under service conditions. Since in many concrete-bridge girders the cracking control

under service loads is the controlling part in the design process, a precise but safe prestress loss prediction method is imperative.

Prestress losses can be defined as a decrease in the initial prestressing force. There are two main types of prestress losses depending on the time of their occurrence. The first is the instantaneous elastic shortening loss and the second type is the long-term losses, mostly due to relaxation of the prestressing strands and creep and shrinkage of the girder concrete and the shrinkage of the deck concrete. Prestress losses are also influenced by other time dependant concrete properties, like its compressive strength and its modulus of elasticity.

Throughout the service life of a prestressed concrete girder, a number of changes occur in the prestressing strands; those changes are presented graphically in Figure 4.1 taken from the NHCRP Report 496 (Tadros et al., 2003). Figure 4.1 also shows that there are some stress gain in the strand due to additional loads applied to the structure, such as, the casting of the concrete deck, and the superimposed dead load (SIDL). The latter consists mainly of the collocation of the concrete barriers that serve as the bridge boundaries.

4.1.1Girder and instrumentation description

For the purpose of this research, long-term prestress losses were monitored in select girders from Bridge 669 located near Farmington, Utah. Bridge 669 is a three span prestress concrete girder bridge. The three spans have lengths of 132.2, 108.5, and 82.2 feet long, respectively. Eleven AASHTO Type VI precast prestressed girders were used to support the deck in each span.

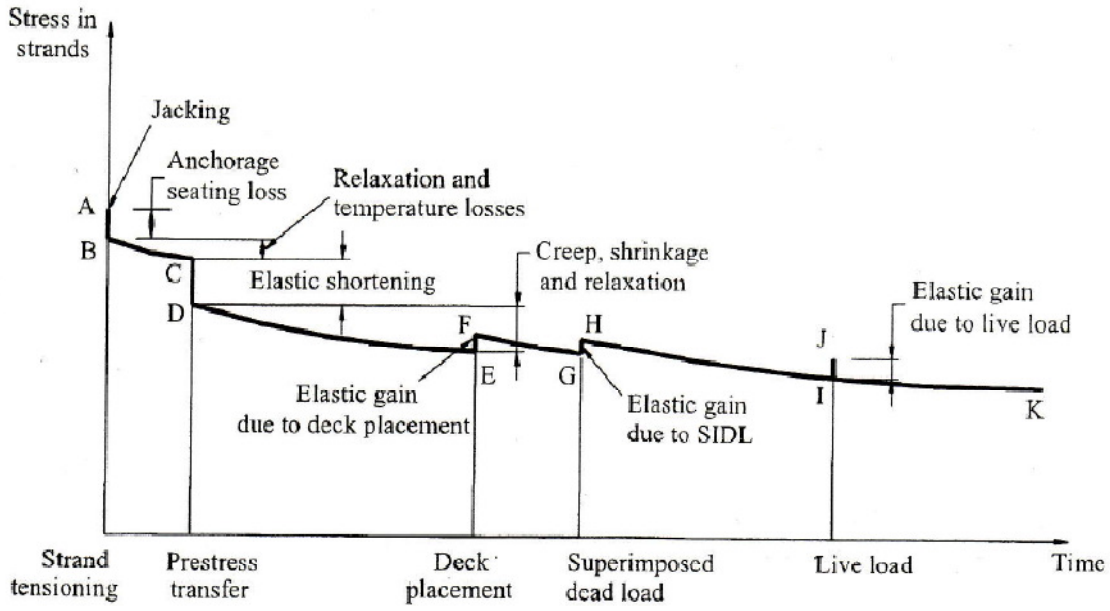

Figure 4.1 Stress in the strands of a prestress concrete girder vs. time (Tadros et al., 2003).

The girders were spaced at 6.9 feet on center, which resulted in a total bridge width of 76.3 feet. The bridge was built on a skew angle of 25˚. The reinforced-concrete deck was constructed as an 8-in. thick cast-in-place slab. The strands used in the girders were 0.5-in. diameter low relaxation strands. An elevation view, as well as, a plan view of the bridge can be seen in Figure 4.2 and Figure 4.3, respectively.

For the scope of this research, select girders were instrumented in the first and third spans. Due to the ease of access of the data collection units attached at the abutments of the bridge located at the beginning of Span 1 and at the end of Span 3. The girders located on the first span (132.2 ft.) required 66 prestressing strands; the girders located in span three (82.2 ft.) required 26 strands. Figure 4.5 shows a cross-sectional view of the prestressing strands for the girders located in the first and third span. In all, three girders from the first and third span, respectively, where instrumented.

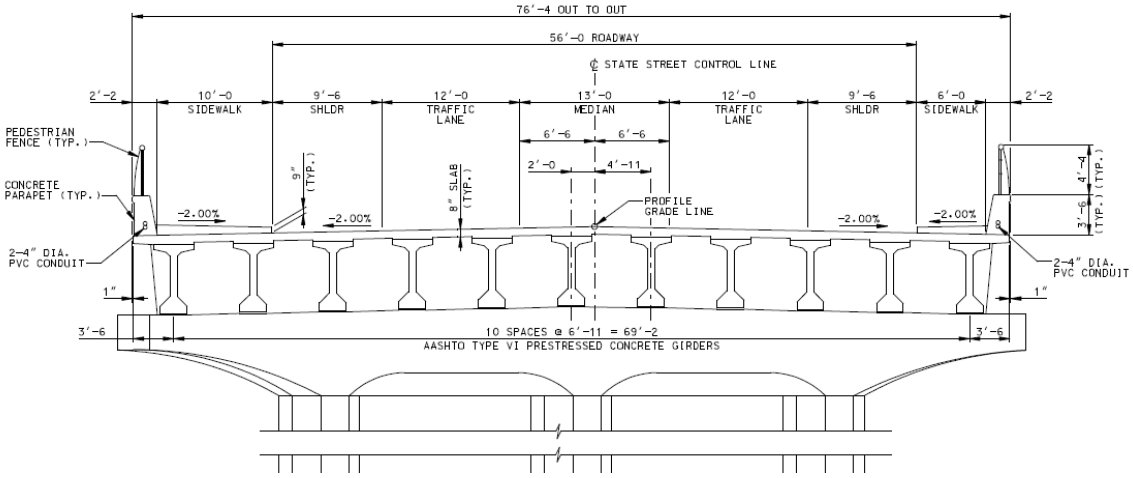

Figure 4.2 Elevation view of Bridge 669.

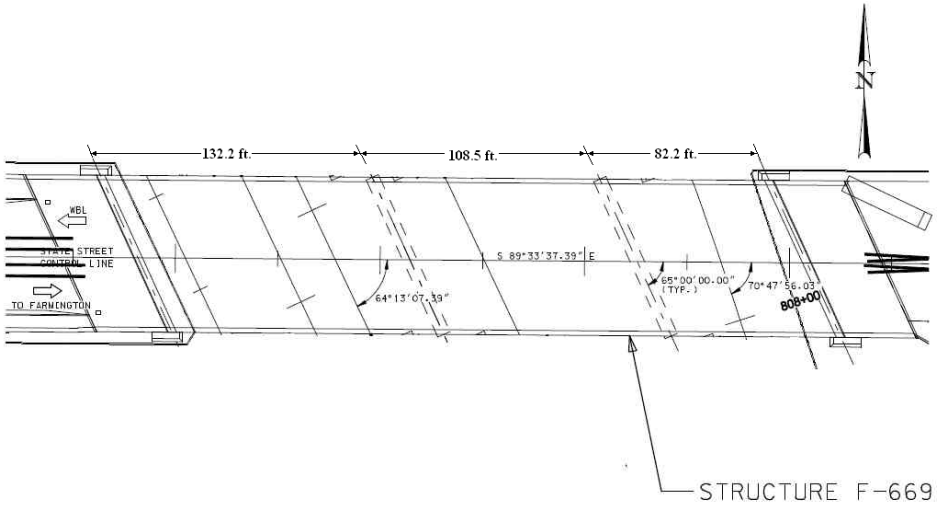

Figure 4.3 Plan view of Bridge 669.

Figure 4.4 669 Bridge looking north.

Twenty-four vibrating wire strain gages (VWSG) were used. The VWSG were installed at midspan of each girder. The location of the VWSGs in each cross section of the girders was as follows: two VWSG were placed at the centroid of the prestressing strands of the girder and two VWSG located at different locations up through the web of the girders. The latter two were placed at 29 and 59 inches from the bottom of the girder.

4.1.2 Prestress loss

With the aid of the VWSG in the centroid of the prestressing strands (Figure 4.7 and Figure 4.8) the strain in the girders was measured. The average of the two VWSG in

each girder was taken. A plot of the average strain in the girders is shown in Figures 4.7 and 4.8 for the 82- and 132-foot-long girders, respectively. As expected the strains are higher on the 132-foot-long girder. The average strain recorded on the last day of readings for the 82-foot-long girder was around 770 με. The average strain recorded for the 132-foot-long girder was in the order of 1100 με.

With the measured strain and the use of Eq. 4.1 the loss in prestress can be calculated. Figures 4.9 and 4.11 show the prestress losses calculated with the use of the Eq. 4.1.

$$\Delta f_{pT} = E_p \Delta \varepsilon_c \tag{4.1}$$

where

Δf_{pT} = the change in steel stress due to total prestress loss.

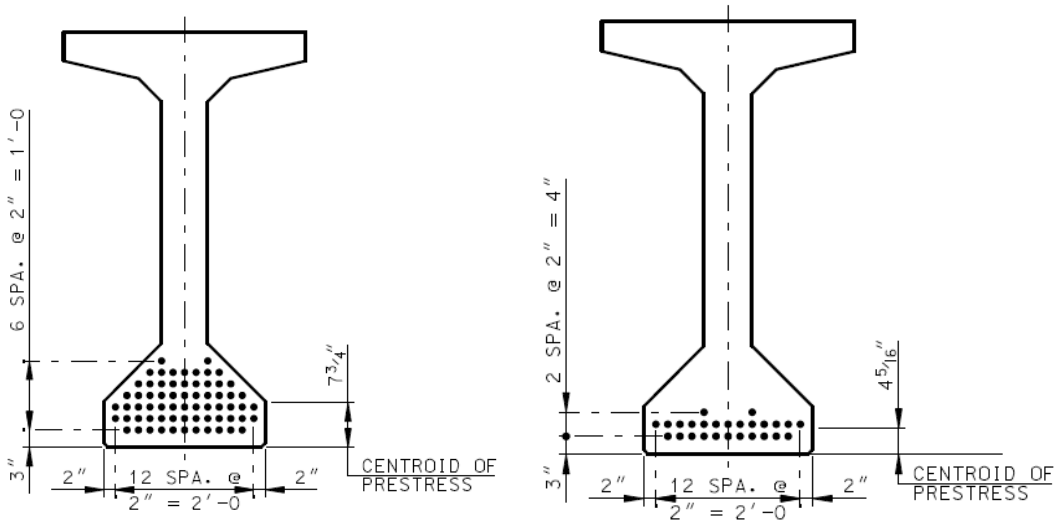

Figure 4.5 Design of the prestressing strands for first and third span girders.

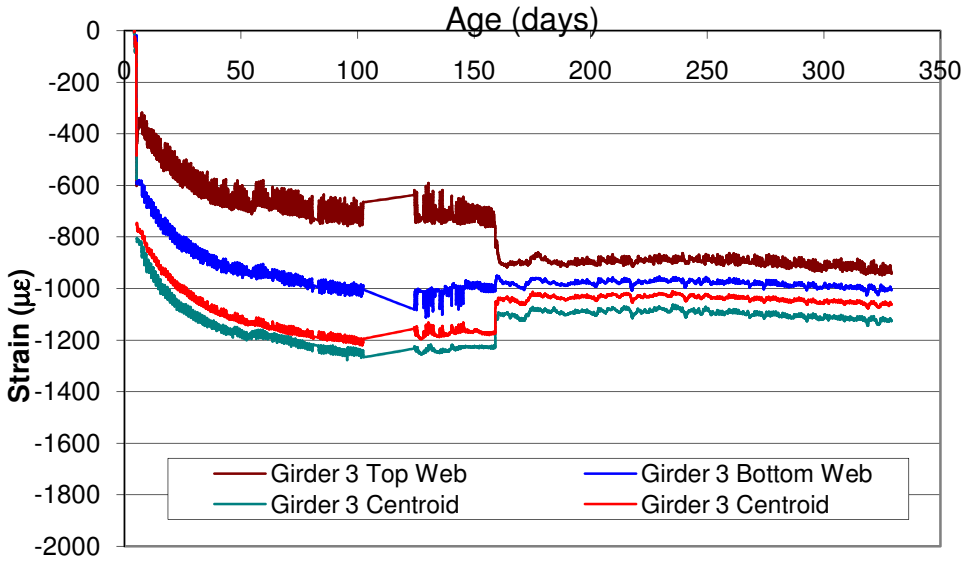

Figure 4.6 Typical strain data from an instrumented girder.

E_p = modulus of elasticity of the prestressing steel (28,500 ksi).

$\Delta\varepsilon_c$ = measured change in strand strain.

On the last day of readings, the average prestress loss for the 82- and 132-foot girders were 21 and 32 ksi, respectively. These prestress losses represent a 10.4 and a 15.8 percent loss of the initial prestressing stress (jacking stress 202.5 ksi), for the 82- and 132-foot-long girders, respectively.

Figures 4.9 and 4.11 present a comparison of the measured prestress losses with the AASHTO LRFD 2004 and 2007 Specifications methods for predicting loss, as well as the refined method in the AASHTO LRFD 2004 Specification.

For the calculations used in the ASSHTO specifications prediction methods, the specified values of the concrete properties were used.

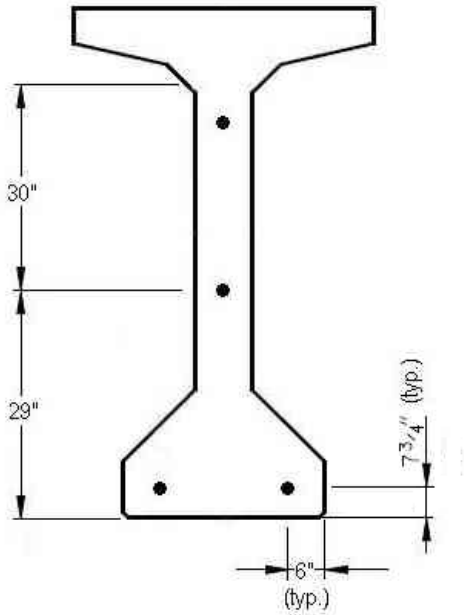

Figure 4.7 Location of the embedded VWSG on the 132-foot girder.

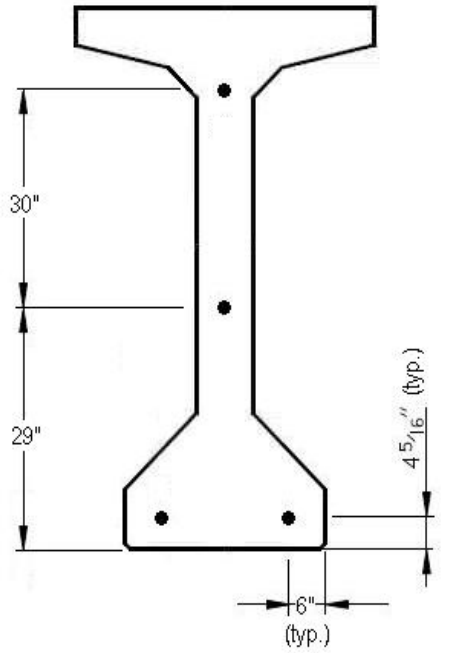

Figure 4.8 Location of the embedded VWSG on the 82-foot girder.

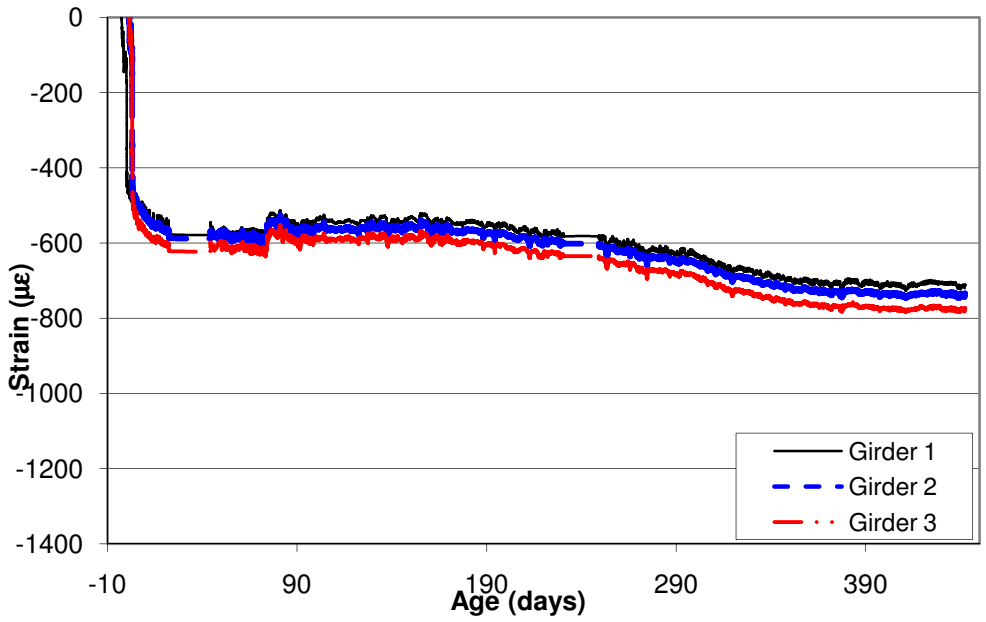

Figure 4.9 Average strain measured in the 82-foot girders.

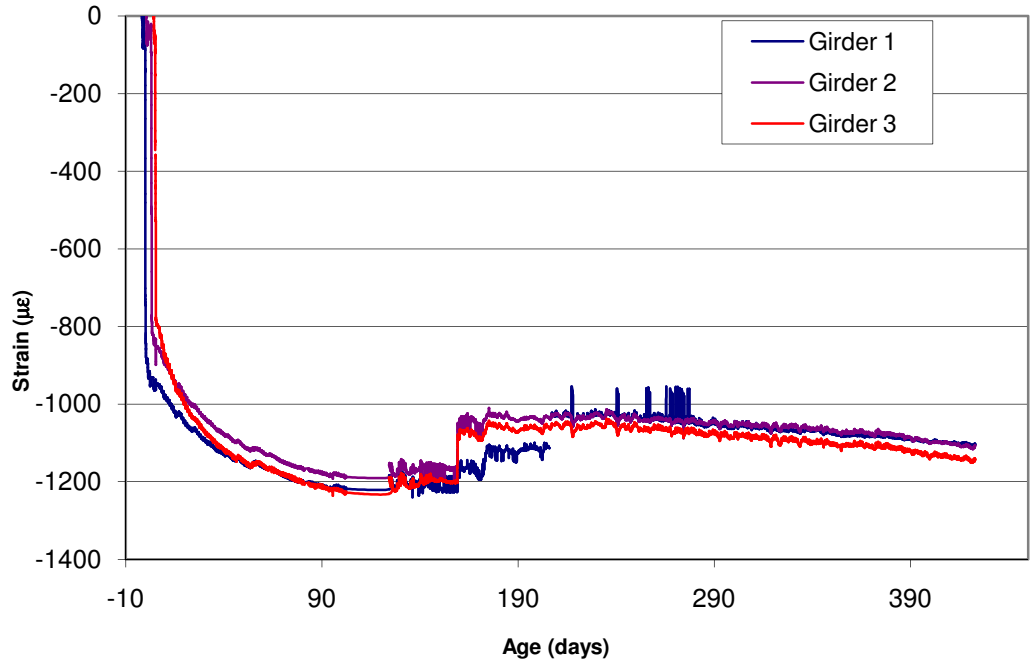

Figure 4.10 Average strain measured in the 132-foot girders.

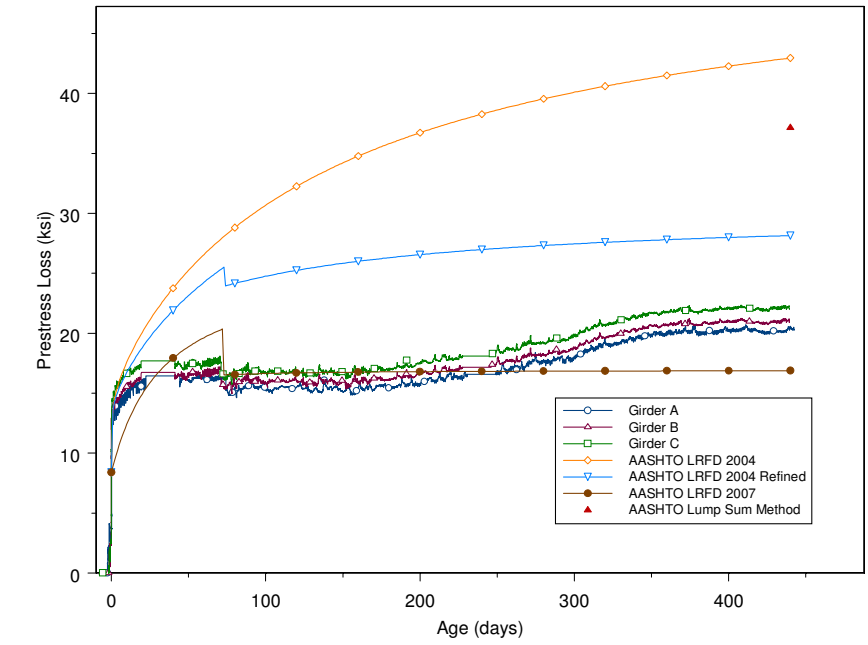

Figure 4.11 Measured vs. predicted prestress loss (using calculated values) for the 82-foot girders.

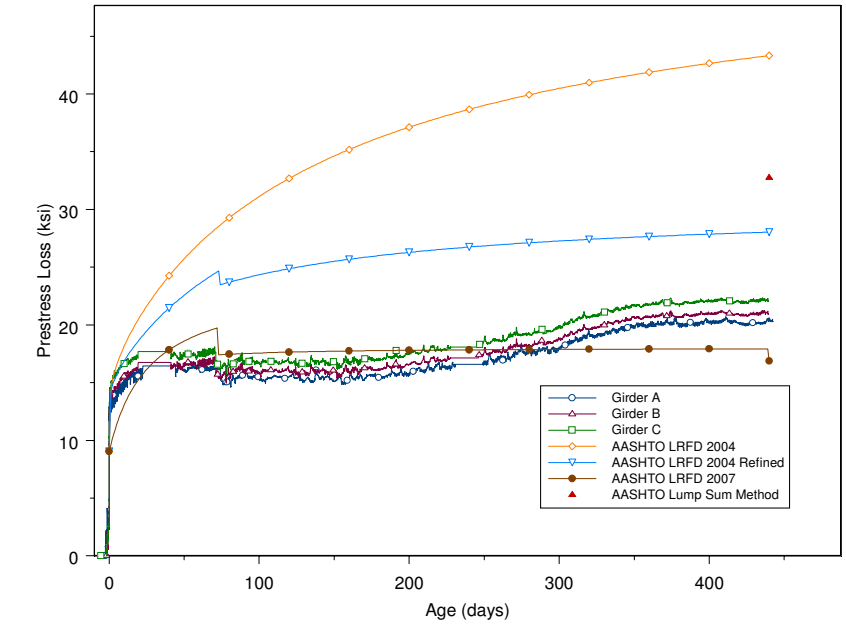

Figure 4.12 Measured vs. predicted prestress loss (using measured values) for the 82-foot girders.

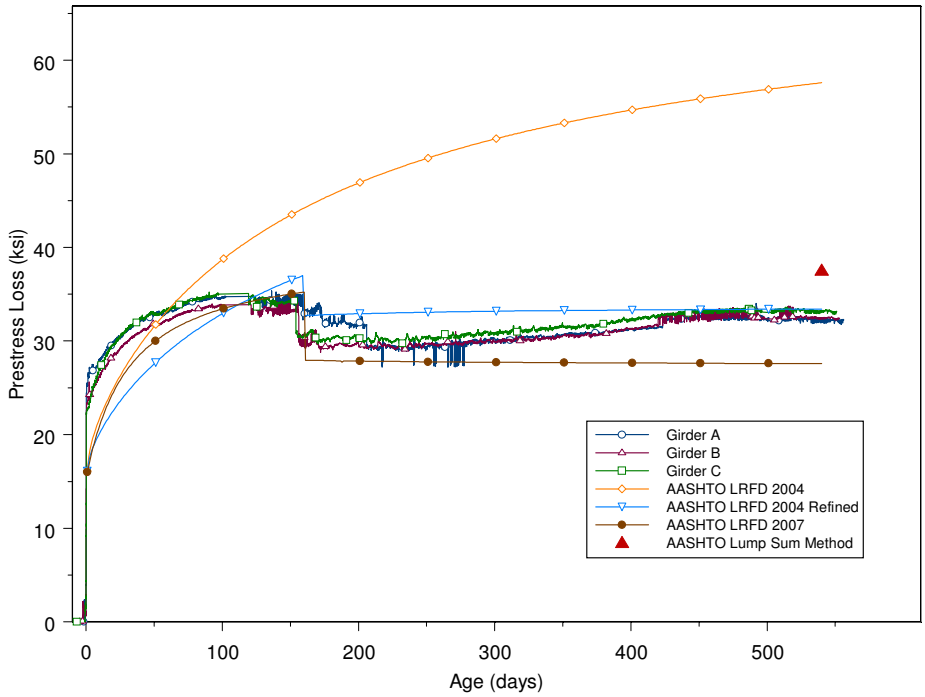

Figure 4.13 Measured vs. predicted prestress loss (using calculated values) for the 132-foot girders.

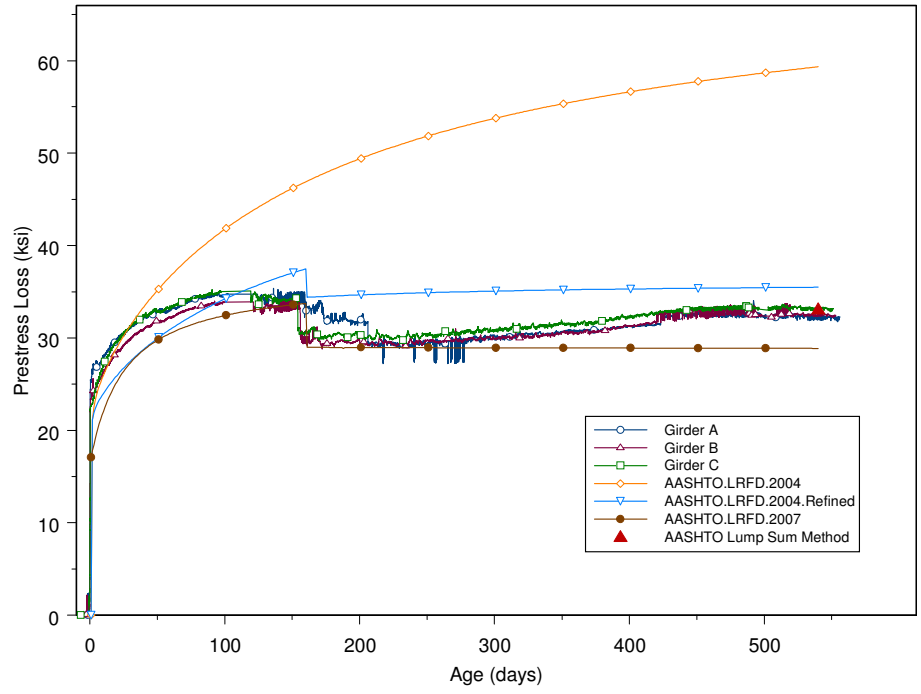

Figure 4.14 Measured vs. predicted prestress loss (using measured values) for the 132-foot girders.

For the 82-foot-long girders, the AASHTO LRFD 2004 specification and the modified 2004 specification overpredicted the prestress loss on the girders (Figure 4.11). The AASHTO LRFD 2007 specification gives a more accurate prediction of the prestress loss for these girders, even though it slightly under predicts the losses. For the 132-foot girders (Figure 4.13) the AASTHO LRFD 2004 also overpredicts the prestress loss. On the other hand, for these girders the AASHTO LRFD 2004 modified and 2007 specifications gives a fairly accurate prediction for the prestress loss. Being the AASHTO LRFD 2004 refined specification the most accurate of the two.

A similar approach is presented in Figures 4.12 and 4.14, but instead of using specified values for the calculations of the predicted prestress losses according to AASHTO LRFD 2004, 2007 and 2004 modified specifications, the measured values presented in Chapter 3 of this research were used. No significant difference was observed, in the 82-foot girder, when the measured values were used for the calculations (Figure 4.13), when compared to the specified values based calculations (Figure 4.14). These comments are also valid for the 132-foot girders, when a comparison between Figures 4.11 and 4.12 is made.

Table 4.1 compares the total prestress loss for the different prediction methods using specified values with the average measured prestress loss for the 132-foot girder. The most accurate method, within 1percent difference with respect to the measured prestress loss, for these girders was the AASHTO Lumped Sum method. AASHTO LRFD 2004 and 2007 gives fairly accurate predictions for the prestress loss.

Similarly, Table 4.2 compares the values of the prediction methods calculated using specified values with the average measured prestress loss for the 82-foot girders.

Once again the AASHTO LRFD 2004 refined and AASHTO LRFD 2007 were within an acceptable range.

Table 4.1 Total calculated (using specified values) and measured prestress loss for the 132-foot girder

Prediction Method	Prestress Loss (ksi)	Percent Difference
AASHTO LRFD 2004	57.8	80%
AASHTO LRFD 2004 Refined	33.4	4%
AASHTO 2007	27.5	-14%
AASHTO Lump Sum	31.7	-1%
Average Measured Data	32.0	

Table 4.2 Total calculated (using specified values) and measured prestress loss for the 82-foot girder

Prediction Method	Prestress Loss (ksi)	Percent Difference
AASHTO LRFD 2004	43.0	105%
AASHTO LRFD 2004 Refined	28.2	34%
AASHTO 2007	16.9	-20%
AASHTO Lump Sum	31.7	51%
Average Measured Data	21.0	

4.2 Measured vs. Predicted Deflections in Prestressed Concrete Bridge Girders

4.2.1 Introduction

Prestressed concrete members are typically more slender than reinforced concrete members. Because of this attribute, the prediction of deflections requires special consideration. For prestressed concrete girders, designed to be fully prestressed, the emphasis must be made in the upward deflection, or camber. Since shrinkage and creep are inherent properties of concrete, this camber may increase with time due to these properties. Camber of bridge girders, may result in invasion of the girder in the road profile, or an irregular surface, in addition, the effects of the permanent dead load and

live load to the final midspan deflection must be investigated to guarantee the members serviceability.

The application of a prestress force, in a simply supported beam, will cause upward camber. Creep, shrinkage and steel relaxation produce a reduction in the camber due to the initial prestress. While prediction of camber may be difficult, due to the time-dependents factors mentioned above, good models are available for calculating the effects of creep and shrinkage on concrete, which permits the calculation of deflections within acceptable ranges of accuracy.

In this chapter, the theoretical basis that served for the development of a MatLab script using the time dependent effects listed in the NCHRP Report 496 and an explanation of the PCI multiplier method is presented. Finally, the calculated results obtained using both these methods are compared to measured values recorded over three years on a typical three-span, prestressed concrete girder bridge.

4.2.2 Prediction methods

4.2.2.1 Detailed time dependent formulation.

The camber in a prestressed concrete girder is dependent on many factors: strands properties and configuration, initial prestress losses due to the relaxation of the strands while the girder is still in the casting yard, time dependent effects due to creep and shrinkage, and the sustained loading due to service and self weight of the structure (Hinkle, 2006).

Several methodologies have been developed by researchers to calculate the girder camber over time. The formulas for calculating the girder camber presented in this section were taken based in the provisions of the NCHRP Report 496. The curvature of the girder was calculated by breaking the girder into 10 equal segments along the total

length of the girder and calculating the curvature at each nodal location. Each of these nodal curvatures were calculated for every time step, taking into account the conditions inherent to each step (i.e. loading conditions, section properties, etc.).

The formula for calculation the total nodal curvature is presented in Eq. 4.2. The total curvature is obtained by subtracting, all the curvatures produced by the loading conditions and time dependent factors, such as creep, shrinkage and relaxation of the prestressing strands from the initial curvature due to the prestress force.

$$\phi_{ti} = \phi_{fpi} - \phi_{g\_selfw.} - \phi_{fp} - \phi_{d\_selfw.} - \phi_{fplongterm} \tag{4.2}$$

where

ϕ_{ti}= Total curvature at time step i.

ϕ_{fpi}= Curvature of the girder due to the initial prestress force.

ϕ_{g_selfw}= Curvature of the girder due to its self weight.

ϕ_{fp}= Curvature of the girder due to the prestress loss at transfer.

ϕ_{d_selfw}= Curvature of the girder due to the self weight of the deck.

$\phi_{fplongterm}$= Curvature of the girder due to prestress loss from deck placement to end of time step.

From elementary mechanics we know that the curvature of any particular cross section is a function of the external moment, modulus of elasticity and moment of inertia, $\phi = M/EI$. Thus all the curvatures calculated using Eq. 4.2 were calculated based on this principle. For any given time and location along the girder, the stress was calculated for the prestressing strands (procedures for calculating stresses are described later on this chapter), then this stress (or sum of stresses) was multiplied by the total strand area, as a

result of this product, a force is obtained. Finally, the prestressing force multiplied by the eccentricity provides an equivalent moment. With this value of moment (M) and the mechanical properties of the girder (EI), a curvature can be calculated. For each load and time – dependent effects, a series of specific calculations must be done. These calculations can be summarized into the following five steps:

1. Calculate the curvature of the girder due to the initial prestress force.

$$\phi_{fpi} = f_{pi} \times A_{ps} \times \frac{e_p}{E_{ci} \times I_{tr\_i}} \tag{4.3}$$

where

ϕ_{fpi}= Curvature due to initial prestress force.

f_{pi}= Initial jacking stress applied to the strands.

A_{ps}=Total cross sectional area of the prestressing strands.

e_p= Distance from centroid of the girder to centroid of prestressing strands based on transformed girder properties.

E_{ci}= Concrete modulus of elasticity at transfer.

I_{tr_i}= Moment of inertia of the transformed section at transfer.

2. Calculate the curvature due to the self weight of the girder.

$$\phi_{g\_selfw} = \frac{M_g}{E_{ci} \times I_{tr\_i}} \tag{4.4}$$

where

ϕ_{g_seflw}= Curvature due to self weight of the girder.

M_g= Moment of the girder due to its self weight.

3. Calculate the curvature due to the prestress loss at time of transfer time:

$$\phi_{fp} = \frac{(\Delta fp_{SR} + \Delta fp_{CR} + \Delta fp_{R2}) \times Aps \times e_{tr\_final}}{I_{bm\_tr\_f} \times E_{ci}} \quad (4.5)$$

where

ϕ_{fp}= Curvature of the girder due to the prestress loss after transfer.

Δfp_{SR}= Prestress loss due to shrinkage at time t_i.

Δfp_{CR}= Prestress loss due to creep at time t_i.

Δfp_{R2}= Prestress loss due to relaxation of the prestressing strands at time t_i.

e_{tr_final}= Distance from centroid of girder to centroid of prestressing strands based on 28 day section properties.

$I_{bm\_tr\_f}$= Moment of inertia of the transformed section at 28 days strength concrete properties.

The prestress loss (in ksi) due to concrete shrinkage between transfer and deck placement is obtained by the Eq. 4-5:

$$\Delta fp_{SR} = \varepsilon_{bid} \times E_p \times K_{id} \quad (4.6)$$

where

ε_{bid}= Girder shrinkage strain from strand transfer to deck placement.

E_p= Modulus of elasticity of the prestressing strands.

K_{id}= Transformed section age – adjusted effective modulus of elasticity factor, for adjustment between transfer and deck placement.

The girder shrinkage strain is then obtained by:

$$\varepsilon_{bid} = 0.00048\left(\frac{5}{1+fci}\right)K_S K_{hs} K_{td} \quad (4.7)$$

$$K_S = 1.45 - 0.13 V/S \quad (4.8)$$

$$K_{hs} = 2.0 - 0.0143H \quad (4.9)$$

$$K_{td} = \frac{t}{61 - 4f_{ci} + t} \quad (4.10)$$

where

K_S= size factor.

V/S= volume to surface ratio of the concrete girder.

K_{hs}= Humidity modification factor.

H= Ambient relative humidity.

K_{td}= Time development factor.

f_{ci}= Concrete's strength at transfer.

t= Age of concrete after loading, in days.

The transformed section age – adjusted effective modulus of elasticity factor is given by

$$K_{id} = \frac{1}{1 + n_i \alpha_{net} \frac{Aps}{Anet}(1 + 0.7\psi_{bif})} \quad (4.11)$$

$$\alpha_{net} = 1 + \frac{A_{net} \times e^2_{pnet}}{I_{net}} \quad (4.12)$$

$$\psi = 1.9 \times K_s \times K_{hc} \times \left(\frac{5}{1+f_{ci}}\right) \times K_{td} \times t_i^{-0.118} \quad (4.13)$$

$$K_{hc} = 1.56 - 0.008H \quad (4.14)$$

where

α_{net}= Initial net section property factor.

Anet= Net section area of the girder.

I_{net}= Net moment of inertia of the girder.

e_{pnet}= Distance from the centroid of the girder to the centroid of the strands based on net section properties.

ψ= Girder creep coefficient.

K_{hc}= Humidity factor for creep coefficient.

Then the prestress loss due to the concrete creep is equal to:

$$\Delta fp_{CR} = n_i \times f_{cgp} \times \psi_{bid} \times K_{id} \tag{4.15}$$

$$f_{cgp} = f_{pi} \times Aps \times \left(\frac{1}{A_{tr\_transfer}} + \frac{e_{p\_tramsfer}^{\ 2}}{I_{tr\_transfer}} \right) - \frac{M_g \times e_{p\_transfer}}{I_{tr\_transfer}} \tag{4.16}$$

where

n_i= Modular ratio at transfer (E_s/E_{ci}).

f_{cgp}= Concrete stress at steel centroid.

f_{pi}= Initial prestress prior to transfer.

$I_{tr\_transfer}$= Moment of inertia of the transformed section at transfer.

$e_{p\_transfer}$= Eccentricity of the prestressing strands relative to the transformed section at transfer.

M_g= Moment due to the self weight of the girder.

In general, the prestress loss due to relaxation of the strands, according to Tadros et al. (2003), is very small, ranging from 1.5 ksi to 4.0 ksi. The researchers recommend that it may be convenient to assume a constant value of 2.4 ksi, equally split between the two time periods: initial to deck placement and deck placement to time infinity. Therefore

for the first part of these calculations, the relaxation losses will be assumed to be constant and can be taken as:

$$\Delta fp_{R2} = 1.2 \tag{4.17}$$

4. Calculate the curvature due to the weight of the deck:

$$\phi_{g\_selfw} = \frac{M_{deck}}{E_c \times I_{bm\_tr\_f}} \tag{4.18}$$

where

M_{deck}= Moment of the girder due to the deck weight.

E_c= Concrete modulus of elasticity at 28 days.

$I_{bm\_tr\_f}$= Moment of inertia of the girder based on 28 day concrete properties.

5. Calculate the long-term curvature:

$$\phi_{longterm} = \frac{\sum \Delta fp_{longterm} \times Aps \times e_{comp\_net}}{E_c \times I_{comp\_net}} \tag{4.19}$$

$$\Delta fp_{longterm} = \Delta fp_{SRD} + \Delta fp_{CRD} + \Delta fp_{R2D} + \Delta fp_{CRDD} + \Delta fp_{SRDD} \tag{4.20}$$

where

Δfp_{SRD}= Prestress loss due to the shrinkage of the girder from deck placement to time infinity.

Δfp_{CRD}= Prestress loss due to the creep of the girder from deck placement to time infinity.

Δfp_{R2D}= Prestress loss due to the relaxation of the strands from deck placement to time infinity.

Δfp_{SRDD}= Prestress loss due to the shrinkage of the deck from its placement to time infinity.

Δfp_{CRDD}= Prestress loss due to the creep of the deck from its placement to time infinity.

e_{comp_net}= Eccentricity of the prestressing strands relative to the centroid of the composite net section.

I_{comp_net}= Moment of inertia of the composite net section.

$$\Delta fp_{SRD} = \varepsilon_{bdf} \times E_s \times k_{df} \tag{4.21}$$

$$\Delta fp_{CRD} = n_i \times f_{Cgp} \times \left(\psi_{bif} - \psi_{bid}\right) \times k_{df} \tag{4.22}$$

$$\Delta fp_{R2D} = 1.2 \tag{4.23}$$

$$\Delta fp_{CRDD} = n \times \left(\left(-\frac{e_{b\_id} \times E_S \times k_{id} \times A_{ps} \times \alpha_{net}}{A_{b\_net}} \right) + \left(-\frac{M_{deck} \times e_{tr\_f}}{I_{tr\_f}} \right) \right) \times \psi_{bdf} \times k_{df} \tag{4.24}$$

$$\Delta fp_{SRDD} = n \times \frac{\varepsilon_{ddf} \times A_d \times E_{cd}}{1 + 0.7\psi_{df}} \times \left(\frac{1}{A_{comp\_net}} + \frac{e_{p\_comp\_net} \times e_{d\_net}}{I_{comp\_net}} \right) \times k_{df} \left(1 + 0.7\psi_{bdf}\right) \tag{4.25}$$

The procedure described above can be easily implemented into a spreadsheet or a MatLab script. For this research, the procedure was coded into a MatLab script so that it can be easily applied to different girder configurations. This script is listed in Appendix A. Once all the nodal curvatures are known, the nodal deflections can be calculated using the Eq. 4.26.

$$\begin{bmatrix} \Delta_1 \\ \Delta_2 \\ \Delta_3 \\ \Delta_4 \\ \Delta_5 \\ \Delta_6 \\ \Delta_7 \\ \Delta_8 \\ \Delta_9 \end{bmatrix} = \frac{(L \times 12)^2}{1000} \begin{bmatrix} 1.5 & 7.33 & 8 & 7 & 6 & 5 & 4 & 3 & 2 & 1 & 0.167 \\ 1.33 & 8 & 14.33 & 14 & 12 & 10 & 8 & 6 & 4 & 2 & 0.333 \\ 1.167 & 7 & 14 & 19.33 & 18 & 15 & 12 & 9 & 6 & 3 & 0.5 \\ 1 & 6 & 12 & 18 & 22.33 & 20 & 16 & 12 & 8 & 4 & 0.667 \\ 0.833 & 5 & 10 & 15 & 20 & 23.33 & 20 & 15 & 10 & 5 & 0.833 \\ 0.667 & 4 & 8 & 12 & 16 & 20 & 22.33 & 18 & 12 & 6 & 1 \\ 0.5 & 3 & 6 & 9 & 12 & 15 & 18 & 19.33 & 14 & 7 & 1.167 \\ 0.333 & 2 & 4 & 6 & 8 & 10 & 12 & 14 & 14.33 & 8 & 1.333 \\ 0.167 & 1 & 2 & 3 & 4 & 5 & 6 & 7 & 8 & 7.33 & 1.5 \end{bmatrix} \begin{Bmatrix} \Phi_0 \\ \Phi_1 \\ \Phi_2 \\ \Phi_3 \\ \Phi_4 \\ \Phi_5 \\ \Phi_6 \\ \Phi_7 \\ \Phi_8 \\ \Phi_9 \\ \Phi_{10} \end{Bmatrix} \tag{4.26}$$

4.2.2.2 PCI multiplier method. This section discusses two simplified methods for calculating camber according the PCI Bridge Design Manual (1997), Chapter 8:

1. Multiplier methods.
2. Improved multiplier methods.

According the multiplier method, first the elastic deflections caused by the effects of prestressing, girder self weight, and other dead loads are calculated using conventional techniques. These changes in camber are multiplied by the appropriate factors selected from Table 4.3 to determine the long term deflections that will occur as a result of time – dependent behavior.

Table 4.3 Suggested PCI multipliers for the multiplier method.

	Without Composite topping	With Composite topping
At erection: 1. Deflection ( ) component - apply to the elastic deflection due to the member weight at the time of release of prestress	1.85	1.85
2. Camber ( ) component - apply to the elastic camber due to prestress at the time of release of prestress	1.80	1.80
Final 3. Deflection ( ) component - apply to the elastic deflection due to the member weight at release of prestress	2.70	2.40
4. Camber ( ) component - apply to the elastic camber due to prestress at the time of release of prestress	2.45	2.20
5. Deflection ( ) component - apply to elastic deflection due to superimposed dead load only	3.00	3.00
6. Deflection ( ) component - apply to elastic deflection caused by the composite topping	----	2.30

An improved multiplier method (Tadros et al., 1985) is similar to the original method described above. However, this method provides improvements, if reliable

estimates are available for the creep coefficient of the actual concrete mix, or if high–performance concrete with a significantly lower creep coefficient is used, these more accurate coefficients may be used. The multipliers for this method are given in Table 4.4. Where

C_u: Ultimate creep coefficient for loads applied immediately after transfer. Average value is 1.88.

C'_u: Ultimate creep coefficient for loads applied at time of erection. Average value is 1.50.

C_a: Creep coefficient for loads applied immediately after transfer and strains measured at time of erection. Average value is 0.96.

α: Time dependent prestress loss at erection divided by total time dependent prestress loss. Average value is 0.60.

χ: Bazant's aging coefficient. Average value is 0.70.

For the purpose of this research, the average values were used in the calculations of the camber using the PCI multipliers methods.

4.2.3 Bridge description

The deflection of several girders from a three span, prestressed, precast concrete girder bridge was monitored for three years. The bridge monitored was the SR18/SR516 in the state of Washington. Fifteen bridge girders were fabricated for the three span bridge. Ten girders from the exterior spans had spans length of 80 ft, and five girders from the middle span had spans length of 137 feet.

Table 4.4 Improved multiplier method coefficients

	Erection Time		Final Time	
Load Condition	Formula	Average	Formula	Average
Initial prestress	$1 + C_a$	1.96	$1 + C_u$	1.96
Prestress loss	$\alpha (1 + \chi C_a)$	1.00	$(1 + \chi C_a)$	1.00
Self weight	$1 + C_a$	1.96	$1 + C_u$	1.96
Dead load on plain beam	1.00	1.00	$1 + C'_u$	2.50
Dead load on plain composite beam	1.00	1.00	$1 + C'_u$	2.50

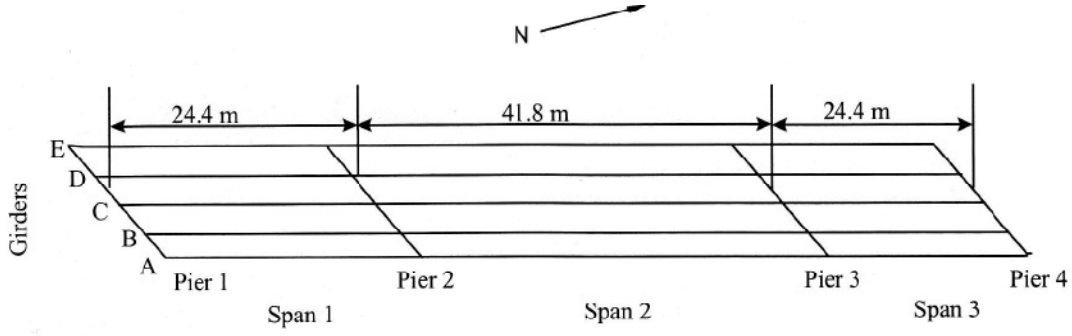

Figure 4.15 Bridge layout.

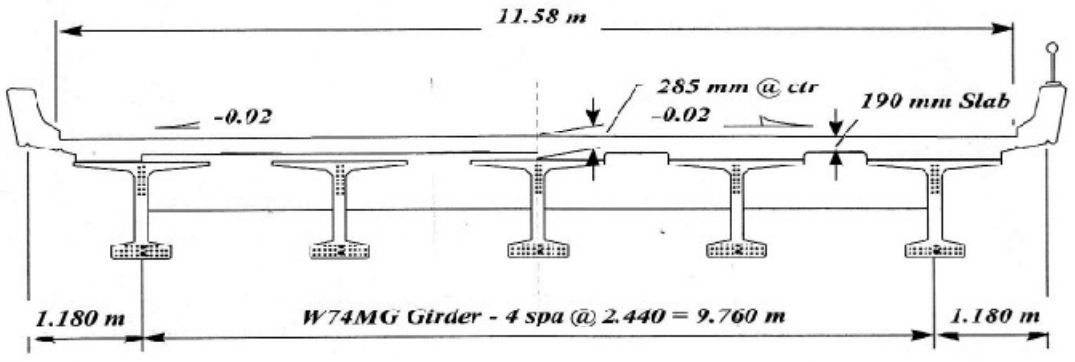

Figure 4.16 Bridge cross section at pier 2 looking north.

The W74MG section was used for each of the girders regardless of the span. The girders were designed as simply supported for girder self weight and three-span continuous for live load. In the field the girders were made composite with a 7.5-in. thick deck. The cross sectional properties for the girder and the composite section are listed in Table 4.5.

Each bridge girder was fabricated with both harped web strands and straight bottom flange strands. The web strands were harped at a distance of 0.4 times the length from each end. Figure 4.17 shows an elevation of one half of one of the girders with the typical tendon strand profile.

Figure 4.18 shows the measured camber for the 137-foot-long girder, whereas Figure 4.19 shows the measured camber for the 80-foot-long girder.

Table 4.5 lists the design details for the bridge girders. The distances from the bottom of the girder to the center of gravity of the harped web strands at the end and at midspan are labeled $W_{eC.G}$ and $W_{mC.G.}$, respectively. The location of the center of gravity of the bottom of the strands is labeled $B_{C.G.}$. For the long girders 14 harped and 26 straight strands were used.

4.2.4 Measured deflection

The girder camber was monitored using two systems. For concentrated measurements over short time periods a stretched-wire system was used. This system used pulleys, weights and a trolley system to provide a reference frame from which to make readings. An LVDT was used to record changes in camber. This LVDT connected to a multiplexer, and the displacements recorded using a data logger.

Table 4.5 Cross section properties

	W74MG Girder	Composite Section
Depth (in)	73.4	80.9
Area (in^2)	752.2	1185.9
I (in^4)	546570.9	961964.8
yb (in)	38.2	52.4
Sb (in^3)	14304.0	18368.0
yt girder (in)	35.2	21.1
St girder (in^3)	15518.0	45694.6
yt slab (in)	-	28.2
St slab (in^3)	-	34185.5

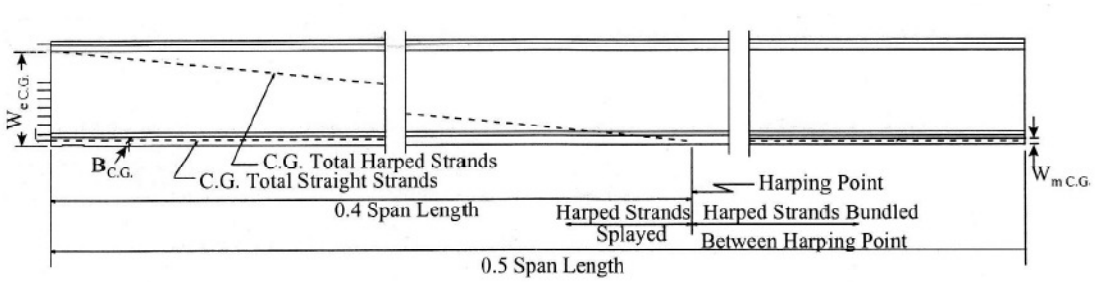

Figure 4.17 Elevation of bridge girders.

The second camber monitoring system consisted in the use of a surveyor's level. Using this system, camber for girders A and C in Span 1 and girders A, B, and C in Span 2 were monitored for three years since casting (Figure 4.15). In addition, Girder B from Span 1 and Girders D and E from Span 2 were monitored starting at erection.

Figure 4.18 shows the measured camber for the 137-foot-long girder, whereas Figure 4.19 shows the measured camber for the 80-foot-long girder.

For the 137-foot-long girders the average measured camber at the time of release was 3.99 in., the largest value of camber was measured in girder 2D with a value of 6.0 in. and the lowest value measured for these long span girders was measured in girder 2A with a camber of 2.5 in.; this difference in the camber at the time of release is most likely to be due to a difference in the curing conditions of the girders while in the casting yard.

Before the deck was placed, the average camber observed on these girders was 5.47 in., after the deck placement, the camber measured was 4.32 in.

The average camber measured in the 80-foot-long girders was 0.51 in., the largest value of camber was observed in girder 1A with a camber of 0.56 in., being the lowest value observed in girder 1B with a camber of 0.49 in. at the time of release. The average camber before the placing of the deck for these girders was 0.78 in. and after the deck placement the average value went to 0.63 in.

Table 4.6 HPC bridge girders design details

Girder	Skew (deg)	Length	56 day f'c (psi)	Release f'c (psi)	# of Harpened Strands	# of Straight Strands	Jacking Stress (psi)	WmC.G. (in)	WeC.G. (in)	BC.G. (in)
Span 1	40	80	10200	5100	6	8	202.5	3.00	53.54	1.87
Span 2	40	137	10200	7500	14	26	202.5	3.37	44.50	3.37
Span 3	40	80	10200	5100	6	8	202.5	3.00	53.54	1.87

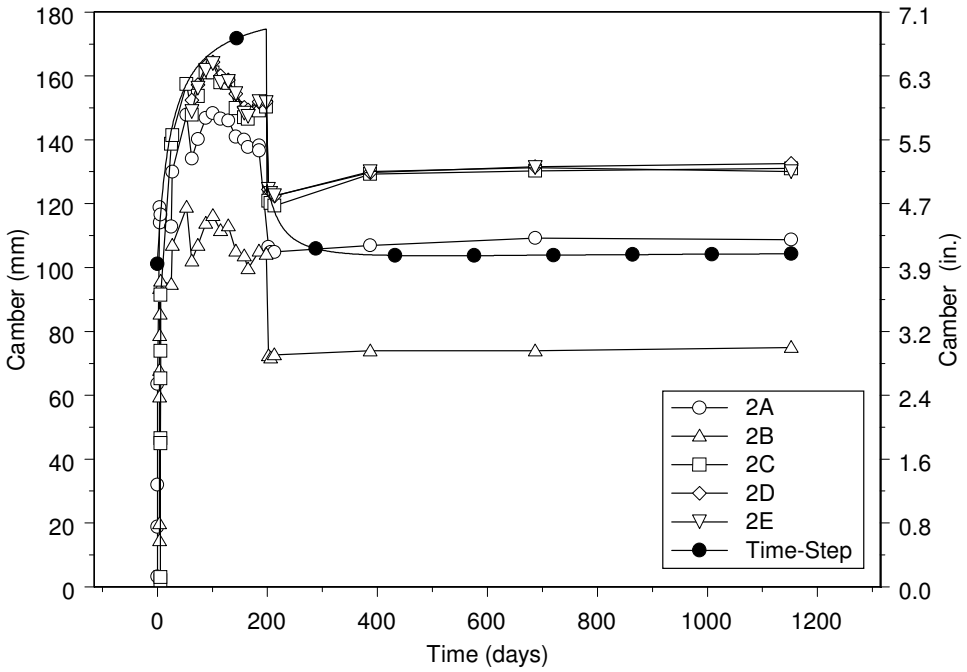

Figure 4.18. Measured camber for the 137-foot-long girder.

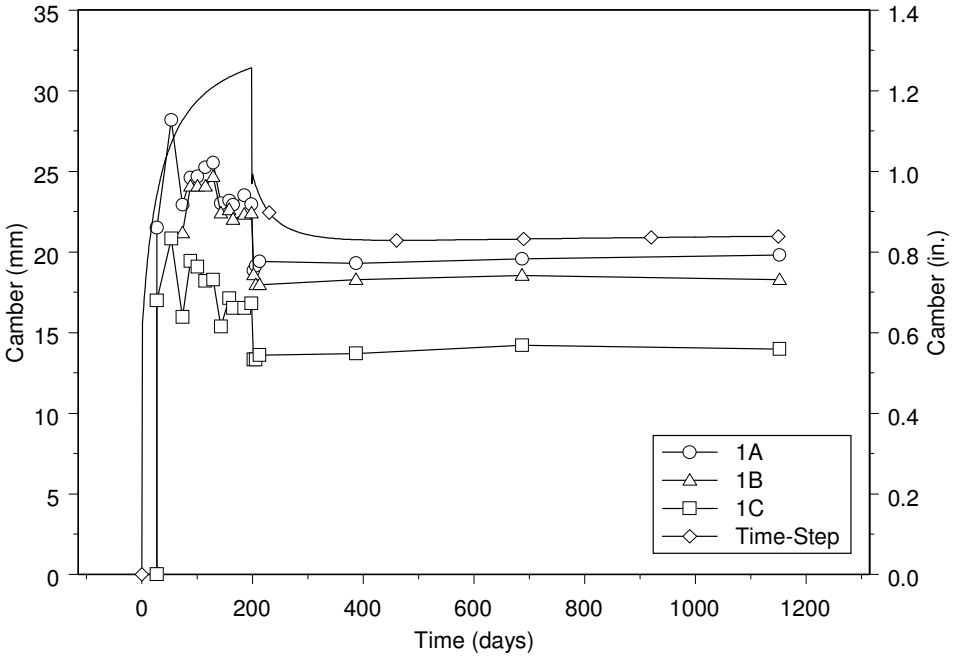

Figure 4.19 Measured camber for the 80-foot-long girders.

4.2.5 Comparison of measured and calculated deflection

In this section, observed and estimated values of camber are compared. The estimated values of camber were calculated following the time-step method, the multiplier method and the improved multiplier method presented in sections 4.2.2.1 and 4.2.2.2, respectively. For all the calculated values of camber, the modulus of elasticity used in the calculations is described by Eq. 4.27. Table 4.7 lists the average girder camber measured for the 80-foot girder with the values calculated using both PCI multipliers methods and the NCHRP Report 496 method.

Table 4.8 compares the average girder camber measured for the 137-foot-long girder with the values calculated using both PCI multipliers methods and the NCHRP Report 496 method.

$$E = \left(40000 \times \sqrt{f'_c}\right)\left(\frac{w}{145}\right)^{1.5} \tag{4.27}$$

In general the PCI simple multiplier method for the Span 1 and Span 2 girders slightly under predicted the camber at release with an average ratio of predicted over measured of 0.96. This method over predicted the camber from transfer until the casting of the deck with a predicted over measured average ratio of 1.33. Finally for the long term camber this method barely over predicted the camber for the long span girder with a ratio of 1.08 of the predicted over the measured. On the other hand this same method under predicted the camber for the short span girder with a ratio of predicted over measured of 0.78.

Table 4.7 Comparison of measured and predicted camber for the 80-foot-long girder

Short Span Girders	Camber (in)			
Method	Release	Before Deck Casting	After Deck Casting	Final
Average Measured	0.51	0.78	0.63	0.67
Multiplier Method	0.50	1.08	0.84	0.72
Improved Multiplier Method	0.50	1.08	0.85	0.90
NCHRP Report 496 Method	0.60	1.24	0.96	0.83

Table 4.8 Comparison of measured and predicted camber for the 137-foot-long girder

Long Span Girders	Camber (in)			
Method	Release	Before Deck Casting	After Deck Casting	Final
Average Measured	3.99	5.47	4.32	4.55
Multiplier Method	3.73	7.04	4.99	3.55
Improved Multiplier Method	3.73	7.55	5.50	5.76
NCHRP Report 496 Method	3.98	6.88	4.95	4.10

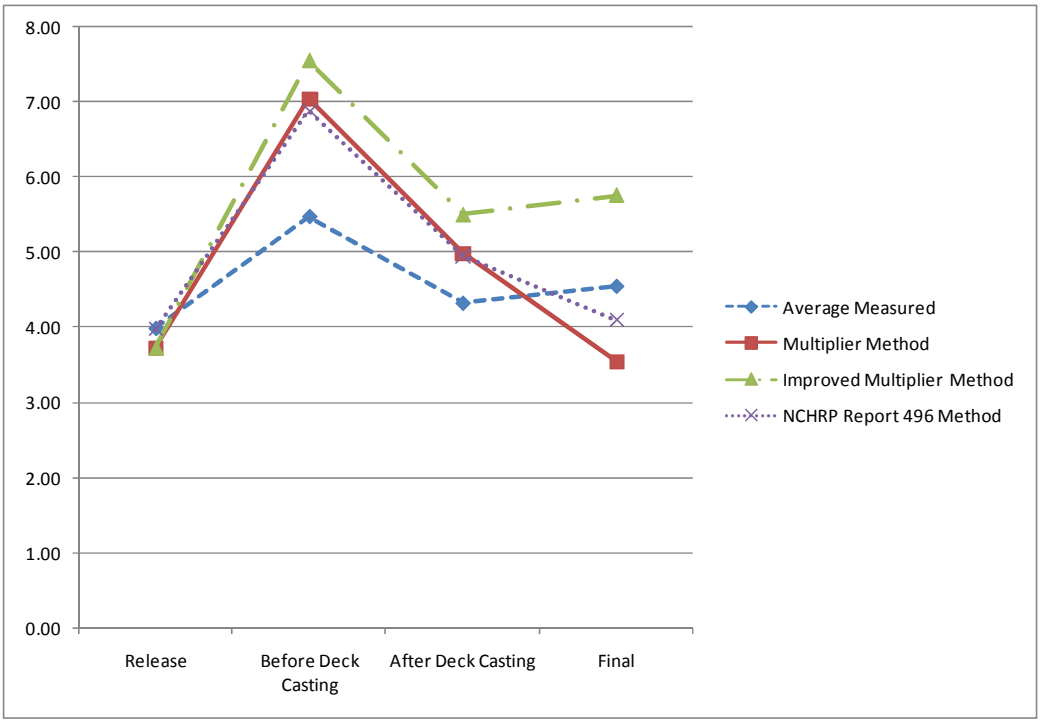

Figure 4.20 Long span girders measured and calculated deflections.

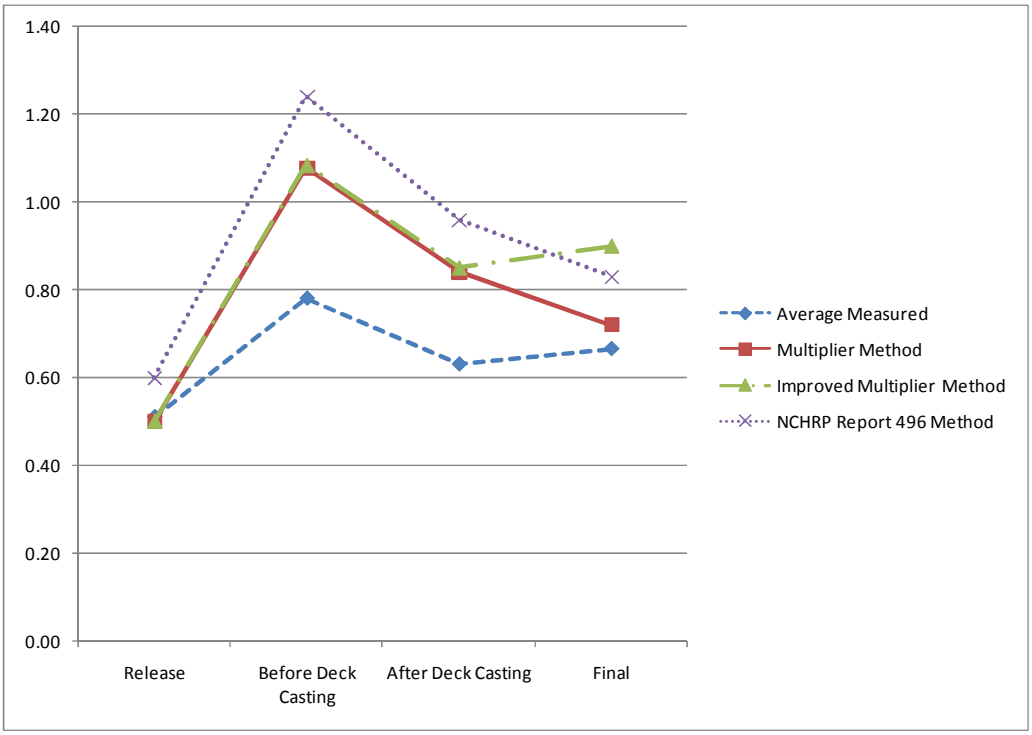

Figure 4.21 Short span girders measured and calculated camber.

The PCI improved multiplier method under predicted the camber at release for both span girders, with a ratio of predicted over measured of 0.96 in average. For the rest of the stages this method over predicted the camber of both span girders.

The NCHRP Report 496 method matched the camber for the short span girder at release, and over predicted it by 18 percent for the long span girder. Thereafter this method over predicted the camber from release to the casting of the deck, and the long term camber too.

CHAPTER 5

CONCLUSIONS

Five laboratory tests were performed on the concrete samples subject of this research in order to characterize the mechanical and physical properties of the concrete. In order to measure the prestress loss of the concrete bridge girders, 6 HPC girders were instrumented with VWSG at the level of the centroid of the prestressing strands. The measured deflections were compared to four prediction methods: AASHTO LRFD 2004 Specifications, AASHTO LRFD 2004 Refined Specifications, AASHTO LRFD 2007 Specifications, and AASHTO Lump Sum method.

The girder camber was monitored using two systems. For concentrated measurements over short time periods a stretched-wire system was used. This system used pulleys, weights and a trolley system to provide a reference frame from which to make readings. An LVDT was used to record changes in camber. The second camber monitoring system consisted in the use of a surveyor's level. The measured camber was compared to predicted camber calculated using the following predictions methods: 1- Time-dependent method described in NCHRP Report 496, 2- PCI Multiplier Method and 3- Improved PCI Multiplier method.

From the results of this research, in both the 82- and 132-foot-long, the AASHTO LRFD 2004 Refined Method does a better job predicting the prestress loss and it can be concluded that all the prediction methods do a better job predicting the loss for the larger girders. The Lump Sum method predicted very accurately the long-term prestress loss for the 132-foot-long girders.

The PCI simple multiplier method for the Span 1 and Span 2 girders slightly under predicted the camber at release with an average ratio of predicted over measured of 0.96. The PCI improved multiplier method under predicted the camber at release for both span girders, with a ratio of predicted over measured of 0.96 in. average. For the rest of the stages this method over predicted the camber of both span girders.

The NCHRP Report 496 method matched the camber for the short span girder at release, and over predicted it by 18 % for the long span girder. Thereafter this method over predicted the camber from release to the casting of the deck, and the long-term camber too.

Further research in short span girders is recommended in order to improve the prediction methods for this type of girders for both prestress loss and deflections prediction models.

The following can be concluded from this research:

1. The 28-day compressive strength for the Eagle precast sample was 12,280 psi, for the 669 Bridge deck sample was 5,796 psi and for the 668 Bridge Deck sample was 5,973 psi.
2. The Secant modulus of elasticity for the Eagle Precast sample at the age of 28 days was 4.85×10^6 psi, for the 669 Bridge deck was 4.389×10^6 psi at the same age and for the 668 Bridge deck was 4.407×10^6 psi.
3. The shrinkage tests performed showed that the strain at 28 days for the Eagle precast concrete reached a value of 351.7×10^{-6} με, for the 669 Bridge deck concrete the strain at 28 days was 533.3×10^{-6} με and for the 668 Bridge deck concrete, at the same age, was 307.2×10^{-6} με.

4. Freeze and thaw test showed very consistent results for all three samples, consisting of Durability Factors around 1 for all three concrete samples.
5. Chloride Ion penetration test showed that the total charge passed through the Eagle precast concrete specimens was 230.8 coulombs, for the 669 Bridge deck concrete specimens was 681.2 coulombs and for the 668 Bridge deck concrete was 832.6 coulombs. All three concrete samples have very low chloride ion permeability.
6. On the last day of readings, the average prestress loss for the 82- and 132-foot-long girders was 21 and 32 ksi, respectively. These prestress losses represent a 10.4 and a 15.8 percent loss of the initial prestressing stress (jacking stress 202.5 ksi), for the 82- and 132-foot-long girders, respectively.
7. For the 132-foot-long girder when comparing the average measured prestress loss with the prediction methods the percent difference for the various methods was as follows: for the AASHTO LRFD 2004 80%, for the AASTHO LRFD 2004 Refined 4%, for the AASHTO LRFD 2007 14%, and for the AASHTO Lump Sum 1%.
8. For the 82-foot-long girder when comparing the average measured prestress loss with the prediction methods the percent difference for the various methods was as follows: for the AASHTO LRFD 2004 105%, for the AASTHO LRFD 2004 Refined 34%, for the AASHTO LRFD 2007 20% and the AASHTO Lump Sum 51%.

REFERENCES

Alexander, M., and Mindess, S. 2005. Aggregates in concrete. New York: Taylor & Francis. 435 p.

American Concrete Institute (ACI). 1982. Prediction of creep, Shrinkage and temperature effects in concrete structures. Detroit: ACI Committee 209.

Bazant, Z. P. 1988. Mathematical modeling of creep and shrinkage of concrete. New York: Wiley. 485 p.

Bazant, Z. P., and Baweja, S. 1995. Justification and refinement of model B3 for concrete creep and shrinkage-1 statistics and sensitivity. Materials and structures 28 (181): 415-430.

Bazant, Z. P., and Chern, J. C. 1984. Double-power logarithmic law for concrete creep. Cement Concrete Resistance. 14: 793-806.

Bazant, Z. P., and Liu, K. L. 1985. Random creep and shrinkage in structures: sampling. Journal of Structural Engineering 111 (5): 1113-1134.

Bazant, Z. P., and Osman, E. 1976. Double power law for basic creep for concrete. Materials and Structures 9 (49): 3-11.

CEB-FIP. 1994. CEB-FIP model code 1990: Design code 1994. London: Thomas Telford. 423 p.

Gardner, N. J., and Lockman, M. J. 2001a. Design provisions for drying shrinkage and creep and normal-strength concrete. Materials journal 98 (2): 159-167.

Gardner, N. J., and Lockman, M. J. 2001b. Discussion of 'design provisions for drying shrinkage and creep of normal-strength concrete. Materials Journal 99 (1): 111.

Goel, R., Kumar, R., and Paul, D. K. 2007. Comparative studies of various creep and shrinkage prediction models for concrete. Journal of materials in civil engineering 19 (3): 249-260.

Higginson, E. C. 1966. Mineral admixtures, significance of tests and properties of concrete and concrete making materials. Philadelphia: ASTM STP 169-A.

Hinkle, S. D. 2006. Investigation of time-dependent deflection in long span, high strength, prestressed concrete bridge beams. Blacksburg: Virginia Polytechnic Institute and State University.

Kang, Y. J. 1989. SPCFRAME-Computer program for nonlinear segmental analysis of planar concrete frames. Berkeley: University of California. 122 p.

Ketchum, M. A. 1986. Redistribution of stress in segmentally erected prestressed concrete bridges. Berkeley: University of California. 158 p.

Li, C. Q., and Melchers, R. E. 1992. Reliability analysis of creep and shrinkage effects. Journal of Structural Engineering 118 (9): 2323-2337.

Madsen, H. O., and Bazant, Z. P. 1983. Uncertainty Analysis of Creep and Shrinkage effects in concrete structures. ACI Journal 80 (2): 116-127.

McMillan, F. R. 1916. Method of designing reinforced concrete slabs. Discussion by A. C. Janni. Trans American Society of Civil Engineers. 80, 1738.

Neville, A. M.1996. Porperties of concrete. New York: John Wiley & Sons, Inc. 779 p.

Nilson, A. 1987. Design of prestressed concrete. New York: John Wiley & Sons, Inc. 592 p.

Oh, B. H., and Lee, H. J. 1996. Time-dependent analysis of reinforced and prestressed concrete structures considering tensile creep of concrete. Procedings, Korea Concrete Institute. 1996, Seoul.

Oh, B. H., and Yang, I. H. 2000. Sensitivity Analysis of Time-Dependent Behavior in PSC box Girder Bridges. Journal of Structural Engineering 126 (2): 171-179.

Precast/Prestressed Concrete Institute (PCI). 1997. Bridge design manual. Chicago: Precast/Prestressed Concrete Institute. 1040 p.

RILEM TC-107-GCS. 1995. Creep and shrinkage prediction models for analysis and design of concrete structures-mode B3. Materials and Structures 28: 357-365.

Russell, H. G., and Larson, S. C. 1989. Thirteen years of deformations in water tower place. ACI Structural Journal 86 (2): 182-191.

Saiidi, M., Hutchens, E., and Gardella, D. 1998. Bridge prestress losses in dry climate. Journal of Bridge Engineering 3 (3): 111-116.

Tadros, M. K., Al-Omaishi, N., Seguirant, S. J., and Gallt, J. G. 2003. Prestress losses in pretensioned high-strength concrete bridge girders. Transportation Research Board, National Cooperative Highway Research Program. Washington, D.C. 63 p.

Teply, B., Kersner, Z., and Novak, D. 1996. Sensitivity study of BPKX and B3 creep and shrinkage models. Materials and Structures 29 (192): 500-505.

Trost, H. 1967. Effects superposition principle on creep and relaxation problems with concrete and prestressed concrete and reinforced concrete construction. 69: 230-238.

Tsubaki, T. 1993. Uncertainty of prediction. 5th International RILEM Symposium (pp. 831-847). Cachan Cedex, France: RILEM.

U.S. Buerau of Reclamation. 1966. Concrete manual. Washington, D.C.: U.S. Government Printing Office.

Waldron, C. J. 2004. Investigation of long-term prestress losses in pretensioned high performance concrete girders. Blacksburg Virginia Polytechnic Institute and State University. 207 p.

Whiting, D. A., Detwiler, R. J., and Lagergren, E. S. 2000. Cracking Tendency and Drying Shrinkage of Silica Fume Concrete for Bridge Deck Applications. Materials Journal 97 (1): 71-78.

APPENDICES

APPENDIX A. Matlab script for camber calculations.

A.1 Script for the long span girder.

```
%Beam Properties
A=752.22; %(in^2)
I=546570.9; %(in^4)
ybbeam=38.19; %(in)
VS=2.89; %(in)
fpi=202.5; %(ksi)
L=137; %(ft)

%Material Properties
H=70; % Humidity (%)
fci=7.5; %(ksi)
fc=10.2; %(ksi)
fcd=5; %(ksi)
w=.14+fc/1000; % (kcf)
w_deck=.14+fcd/1000;%(kcf)
Es=28500; %(ksi)
Eci=((40000*(fci*1000)^.5+10^6)*(w/.14)^1.5)/1000; % (ksi)
Ec=((40000*(fci*1000)^.5+10^6)*(w/.14)^1.5)/1000; %(ksi)
Ecd=33000*w_deck^1.5*fcd^.5;%(ksi)
ni=Es/Eci;
n=Es/Ec;
n_deck=Ecd/Ec;
Aps=40*.217;
%Area of prestressing strands (in^2)
ypb=[17.77  14.17 10.57 6.97  3.37  3.37  3.37  6.97  10.57 14.17
      17.77];
%centroid of prestressing strands (in)

%Composite & deck Properties
t=7.5; % (in) Thickness
width=96; %(in) slab width
ybdeck=77.18; %(in)
ha_t=0; % haunch thickness (in)
ha_w=48.2; % haunch width (in)
VSd=((t*width)+(ha_t*ha_w))/(2*(t+width+ha_t)); %Volume/surface (in)

%Time data input.
ti=1;%time to release (d)
td=56; % Time to deck placement (d)
tf=2000; % Time at final (d)

x=0:.1*L:L;
Atr=A+((ni-1)*Aps);
Atr_final=A+((n-1)*Aps);
Anet=A-Aps;
yb_net=((A*ybbeam)-(Aps*ypb))/Anet;
yb=((A*ybbeam)+((ni-1)*Aps*ypb))/Atr;
yb_tr_final=((A*ybbeam)+((n-1)*Aps*ypb))/Atr_final;
ep=yb-ypb;
ep_net=yb_net-ypb;
ep_tr_final=yb_tr_final-ypb;
Itr=I+A*(yb-ybbeam).^2+(ni-1)*Aps*(yb-ypb).^2;%Transformed moment
%of inertia.
Inet=I+A*(yb_net-ybbeam).^2-Aps*(yb_net-ypb).^2;%Net moment of inertia
Itr_final=I+A*(yb-ybbeam).^2+(n-1)*Aps*(yb_tr_final-ypb).^2;
```

```
A_deck=((t*width)+(ha_t*ha_w))*n_deck;
ybd=((t*width*ybdeck)+(ha_t*ha_w*(ybdeck-ha_t/2-t/2)))*n_deck/A_deck;
I_deck=(((width*t^3/12)+(t*width*(ybdeck-
ybd)^2))+((ha_w*ha_t^3/12)+ha_t*ha_w*(ybdeck-ha_t/2-t/2-ybd)))*n_deck;
A_comp_g=A+A_deck;
yb_comp_g=(A*ybbeam+A_deck*ybd)/A_comp_g;
I_comp_g=I+I_deck+A*(ybbeam-yb_comp_g)^2+(ybd-yb_comp_g)^2;
ep_comp_g=yb_comp_g-ypb;
ed_comp_g=yb_comp_g-ybd;
alpha_comp_g=1+A_comp_g*ep_comp_g.^2./I_comp_g;
A_comp_net=Anet+A_deck;
yb_comp_net=((Anet*yb_net)+(A_deck*ybd))/A_comp_net;
I_comp_net=Inet+I_deck+Anet*(yb_net-yb_comp_net).^2+A_deck*(ybd-
yb_comp_net).^2;
ep_comp_net=yb_comp_net-ypb;
ed_comp_net=yb_comp_net-ybd;
alpha_comp_net=1+A_comp_net*ep_comp_net.^2./I_comp_net;
A_comp_tr=Atr_final+A_deck;
yb_comp_tr=(Atr_final*yb_tr_final+A_deck*ybd)/A_comp_tr;
I_comp_tr=Itr_final+I_deck+Atr_final*(yb_tr_final-
yb_comp_tr).^2+A_deck*(ybd-yb_comp_tr).^2;
ep_comp_tr=yb_comp_tr-ypb;
alpha_comp_tr=1+A_comp_tr*ep_comp_tr.^2./I_comp_tr;


curv_ip=(fpi/Eci)*Aps.*ep./Itr;%curvature due to initial prestress.

W=A/144*w; %Unit load due to selfweight.
M=(W/2*(L*x-x.^2))*12;

curv_w=-M./Itr/Eci;%curvature due to selfweight;

defl=(L*12)^2/1000*[1.5 7.33333 8 7 6 5 4 3 2 1 0.16667;
    1.33333 8 14.33333 14 12 10 8 6 4 2 0.33333;
    1.16667 7 14 19.33333 18 15 12 9 6 3 0.5;
    1 6 12 18 22.33333 20 16 12 8 4 0.66667;
    0.83333 5 10 15 20 23.33333 20 15 10 5 0.83333;
    0.66667 4 8 12 16 20 22.33333 18 12 6 1;
    0.5 3 6 9 12 15 18 19.33333 14 7 1.16667;
    0.33333 2 4 6 8 10 12 14 14.33333 8 1.33333;
    0.16667 1 2 3 4 5 6 7 8 7.33333 1.5];

drel=defl*curv_ip' + defl*curv_w';%deflection at release (in)
camber_rel=[0 drel' 0];
figure(1)
plot(x,camber_rel);grid on
xlabel('Length (ft)')
ylabel('Camber (in)')
title('Camber at release')

K_s=(1064-94*VS)/735;%Volume surface ratio factor
K_sd=(1064-94*VSd)/735;
K_hs=2.0-0.0143*H;% Humidity correction factor
K_hc=1.56-.008*H;
for i=0:1:td-ti
    K_tdid(1,i+1)=i/(61-4*fci+i); %#ok<AGROW>
end
for i=td+1:1:tf
    K_tddf(1,(i-td))=(i-td)/(61-4*fci+(i-td)); %#ok<AGROW>
end
for i=td+1:1:tf
    K_tdddf(1,(i-td))=(i-td)/(61-4*fcd+(i-td)); %#ok<AGROW>
end
for i=td:1:tf-1
```

```
    K_tdif1(1,((i-td)+1))=i/(61-4*fci+i); %#ok<AGROW>
end
K_tdif=(tf-ti)/(61-4*fci+(tf-ti));
alpha_net=1+((Anet*ep_net.^2)./Inet);
y=1.9*K_s*K_hc*(5/(1+fci))*ti^-0.118;
ybid=y*K_tdid;
ybif=y*K_tdif;
ybif1=y*K_tdif1;
ybdf=1.9*K_s*K_hc*(5/(1+fci))*td^-0.118*K_tddf;
ydf=1.9*K_sd*K_hc*(5/(1+fcd))*ti^-0.118*K_tdddf;
Kid=1./(1+ni*alpha_net*Aps/Anet*(1+.7*ybif));
Kdf=1./(1+ni*alpha_comp_net*Aps/A_comp_net*(1+.7*ybif));
e_bid=.00048*(5/(1+fci))*K_s*K_hs*K_tdid;
e_ddf=.00048*(5/(1+fcd))*K_sd*K_hs*K_tdddf;
e_bif=.00048*(5/(1+fci))*K_s*K_hs*K_tddf;
e_bdf=e_bif-e_bid(1,length(e_bid));
fcgp=fpi*Aps*(1/Atr+(ep.^2./Itr))-(M.*ep./Itr);
for i=1:1:length(ybid)
    for m=1:1:11;
delta_fp_cr(i,m)=ni*fcgp(1,m)*ybid(1,i)*Kid(1,m); %#ok<AGROW>
    end
end
for i=1:1:length(e_bid)
    for m=1:1:11
        delta_fp_sr(i,m)=e_bid(1,i)*Es*Kid(1,m); %#ok<AGROW>
    end
end
for i=1:1:td-ti+1
    for m=1:1:11
delta_fp_r(i,m)=1.2; %#ok<AGROW>
    end
end
loss_id=delta_fp_r+delta_fp_cr+delta_fp_sr;
for i=1:1:td
    for m=1:1:11
        curv_id(i,m)=-
loss_id(i,m)*Aps*ep_tr_final(1,m)/Itr_final(1,m)/Eci; %#ok<AGROW>
    end
end
Wdeck=((t*width)+(ha_t*ha_w))/144*.15;
Mdeck=Wdeck/2*(L*x-x.^2)*12;
Madl=[0.00  0.00  0.00  0.00  0.00  0.00  0.00  0.00  0.00  0.00
      0.00];
curv_deck=-Mdeck/Ec./Itr_final;
for i=1:1:length(curv_id)
    did(:,i)=defl*curv_id(i,:)';  %#ok<AGROW>
end
z=zeros(length(curv_id),1);
camber_id=[z did' z];
for i=1:1:length(camber_id)
    for m=1:1:11

camber_at_deck(i,m)=camber_rel(1,m)*(1+ybid(1,i))+camber_id(i,m)*(1+0.7
*ybid(1,i));  %#ok<AGROW>
    end
end
defl_due_deck=defl*curv_deck';
camber_deck=[0 defl_due_deck' 0];
camber_net_deck=camber_at_deck(length(camber_at_deck),:)+camber_deck;
time=0:1:td-1;
camber_at_deck(length(camber_at_deck),:)=camber_net_deck;
for i=1:1:length(K_tdddf)
    for m=1:1:11
```

```
        SR_deck(i,m)=-
n*e_ddf(1,i)*t*width*Ecd/(1+0.7*ydf(1,i))*((1/A_comp_net)+(ep_comp_net(
1,m)*ed_comp_net(1,m))/I_comp_net(1,m)); %#ok<AGROW>
    end
end
for i=1:1:length(e_bdf)
    for m=1:1:11
        SR_bdf(i,m)=-e_bdf(1,i)*Es*Kdf(1,m); %#ok<AGROW>
    end
end
for i=1:1:length(ybif1)
    for m=1:1:11
        CR_df(i,m)=-ni*fcgp(1,m)*(ybif1(1,i)-
ybid(1,length(ybid)))*Kdf(1,m); %#ok<AGROW>
    end
end
longterm_id=-loss_id(length(loss_id),:)*Aps.*alpha_net/Anet;
k57=-Mdeck.*ep_tr_final./Itr_final-Madl.*ep_comp_tr./I_comp_tr;
sum=longterm_id+k57;
for i=1:1:length(ybdf)
    for m=1:1:11
        CR_b(i,m)=-n*sum(1,m)*ybdf(1,i)*Kdf(1,m); %#ok<AGROW>
    end
end
longterm_df=CR_b+CR_df+SR_bdf+SR_deck-1.2;

for i=1:1:length(longterm_df)
    for j=1:1:11

curv_longterm(i,j)=longterm_df(i,j)*Aps*ep_comp_net(1,j)/I_comp_net(1,j
)/Ec; %#ok<AGROW>
    end
end
for i=1:1:length(curv_longterm)
    def_longterm(:,i)=defl*curv_longterm(i,:)'; %#ok<AGROW>
end
z1=zeros(length(def_longterm),1);
camber_longterm=[z1 def_longterm' z1];
curv_dl_comp=-Madl./I_comp_tr/Ec;
dfl_due_dl_comp=defl*curv_dl_comp';
camber_dl_comp=[0 dfl_due_dl_comp' 0];
for i=1:1:length(camber_longterm)
    for j=1:1:11

camber_final(i,j)=(camber_rel(1,j)*(1+ybif1(1,i)))+(camber_id(length(ca
mber_id),j)*(1+0.7*ybif1(1,i)))+(camber_deck(1,j)*(1+ybdf(1,i)))+(cambe
r_dl_comp(1,j)*(1+ybdf(1,i)))+(camber_longterm(i,j)*(1+.7*ybdf(1,i)));
    end
end

camber_if=[camber_at_deck; camber_final];
time_final=[time td:1:tf-1];
figure(2)
plot(time,camber_at_deck(:,6)');grid on
xlabel('Beam Age (d)')
ylabel('Camber (in)')
title('Midspan Camber, initial to deck placement')
figure(3)
plot(x,camber_net_deck);grid on
xlabel('Length (ft)')
ylabel('Camber (in)')
title('Net Camber after deck placement')
total_camber=[camber_at_deck; camber_net_deck];
figure(4)
```

```
plot(time,camber_at_deck(:,6));grid on
xlabel('Beam Age (d)')
ylabel('Camber (in)')
title('Midspan Camber, initial to deck placement')
figure(5)
plot(time_final,camber_if(:,6)');grid on
xlabel('Beam Age (d)')
ylabel('Camber (in)')
title('Midspan Camber, initial to final*')
```

A.2 Script for the short span girder.

```
%Beam Properties
A=752.22; %(in^2)
I=546570.9; %(in^4)
ybbeam=38.19; %(in)
VS=2.89; %(in)
fpi=202.5; %(ksi)
L=137; %(ft)

%Material Properties
H=70; % Humidity (%)
fci=7.5; %(ksi)
fc=10.2; %(ksi)
fcd=5; %(ksi)
w=.14+fc/1000; % (kcf)
w_deck=.14+fcd/1000;%(kcf)
Es=28500; %(ksi)
Eci=((40000*(fci*1000)^.5+10^6)*(w/.14)^1.5)/1000; % (ksi)
Ec=((40000*(fci*1000)^.5+10^6)*(w/.14)^1.5)/1000; %(ksi)
Ecd=33000*w_deck^1.5*fcd^.5;%(ksi)
ni=Es/Eci;
n=Es/Ec;
n_deck=Ecd/Ec;
Aps=40*.217;
%Area of prestressing strands (in^2)
ypb=[17.77  14.17 10.57 6.97  3.37  3.37  3.37  6.97  10.57 14.17
      17.77];
%centroid of prestressing strands (in)

%Composite & deck Properties
t=7.5; % (in) Thickness
width=96; %(in) slab width
ybdeck=77.18; %(in)
ha_t=0; % haunch thickness (in)
ha_w=48.2; % haunch width (in)
VSd=((t*width)+(ha_t*ha_w))/(2*(t+width+ha_t)); %Volume/surface (in)

%Time data input.
ti=1;%time to release (d)
td=56; % Time to deck placement (d)
tf=2000; % Time at final (d)

x=0:.1*L:L;
Atr=A+((ni-1)*Aps);
Atr_final=A+((n-1)*Aps);
Anet=A-Aps;
yb_net=((A*ybbeam)-(Aps*ypb))/Anet;
yb=((A*ybbeam)+((ni-1)*Aps*ypb))/Atr;
yb_tr_final=((A*ybbeam)+((n-1)*Aps*ypb))/Atr_final;
ep=yb-ypb;
ep_net=yb_net-ypb;
ep_tr_final=yb_tr_final-ypb;
Itr=I+A*(yb-ybbeam).^2+(ni-1)*Aps*(yb-ypb).^2;%Transformed moment
%of inertia.
Inet=I+A*(yb_net-ybbeam).^2-Aps*(yb_net-ypb).^2;%Net moment of inertia
Itr_final=I+A*(yb-ybbeam).^2+(n-1)*Aps*(yb_tr_final-ypb).^2;
A_deck=((t*width)+(ha_t*ha_w))*n_deck;
ybd=((t*width*ybdeck)+(ha_t*ha_w*(ybdeck-ha_t/2-t/2)))*n_deck/A_deck;
I_deck=(((width*t^3/12)+(t*width*(ybdeck-
ybd)^2))+((ha_w*ha_t^3/12)+ha_t*ha_w*(ybdeck-ha_t/2-t/2-ybd)))*n_deck;
A_comp_g=A+A_deck;
yb_comp_g=(A*ybbeam+A_deck*ybd)/A_comp_g;
```

```
I_comp_g=I+I_deck+A*(ybbeam-yb_comp_g)^2+(ybd-yb_comp_g)^2;
ep_comp_g=yb_comp_g-ypb;
ed_comp_g=yb_comp_g-ybd;
alpha_comp_g=1+A_comp_g*ep_comp_g.^2./I_comp_g;
A_comp_net=Anet+A_deck;
yb_comp_net=((Anet*yb_net)+(A_deck*ybd))/A_comp_net;
I_comp_net=Inet+I_deck+Anet*(yb_net-yb_comp_net).^2+A_deck*(ybd-
yb_comp_net).^2;
ep_comp_net=yb_comp_net-ypb;
ed_comp_net=yb_comp_net-ybd;
alpha_comp_net=1+A_comp_net*ep_comp_net.^2./I_comp_net;
A_comp_tr=Atr_final+A_deck;
yb_comp_tr=(Atr_final*yb_tr_final+A_deck*ybd)/A_comp_tr;
I_comp_tr=Itr_final+I_deck+Atr_final*(yb_tr_final-
yb_comp_tr).^2+A_deck*(ybd-yb_comp_tr).^2;
ep_comp_tr=yb_comp_tr-ypb;
alpha_comp_tr=1+A_comp_tr*ep_comp_tr.^2./I_comp_tr;


curv_ip=(fpi/Eci)*Aps.*ep./Itr;%curvature due to initial prestress.

W=A/144*w; %Unit load due to selfweight.
M=(W/2*(L*x-x.^2))*12;

curv_w=-M./Itr/Eci;%curvature due to selfweight;

defl=(L*12)^2/1000*[1.5 7.33333 8 7 6 5 4 3 2 1 0.16667;
    1.33333 8 14.33333 14 12 10 8 6 4 2 0.33333;
    1.16667 7 14 19.33333 18 15 12 9 6 3 0.5;
    1 6 12 18 22.33333 20 16 12 8 4 0.66667;
    0.83333 5 10 15 20 23.33333 20 15 10 5 0.83333;
    0.66667 4 8 12 16 20 22.33333 18 12 6 1;
    0.5 3 6 9 12 15 18 19.33333 14 7 1.16667;
    0.33333 2 4 6 8 10 12 14 14.33333 8 1.33333;
    0.16667 1 2 3 4 5 6 7 8 7.33333 1.5];

drel=defl*curv_ip' + defl*curv_w';%deflection at release (in)
camber_rel=[0 drel' 0];
figure(1)
plot(x,camber_rel);grid on
xlabel('Length (ft)')
ylabel('Camber (in)')
title('Camber at release')

K_s=(1064-94*VS)/735;%Volume surface ratio factor
K_sd=(1064-94*VSd)/735;
K_hs=2.0-0.0143*H;% Humidity correction factor
K_hc=1.56-.008*H;
for i=0:1:td-ti
    K_tdid(1,i+1)=i/(61-4*fci+i); %#ok<AGROW>
end
for i=td+1:1:tf
    K_tddf(1,(i-td))=(i-td)/(61-4*fci+(i-td)); %#ok<AGROW>
end
for i=td+1:1:tf
    K_tdddf(1,(i-td))=(i-td)/(61-4*fcd+(i-td)); %#ok<AGROW>
end
for i=td:1:tf-1
    K_tdif1(1,((i-td)+1))=i/(61-4*fci+i); %#ok<AGROW>
end
K_tdif=(tf-ti)/(61-4*fci+(tf-ti));
alpha_net=1+((Anet*ep_net.^2)./Inet);
y=1.9*K_s*K_hc*(5/(1+fci))*ti^-0.118;
ybid=y*K_tdid;
```

```
ybif=y*K_tdif;
ybif1=y*K_tdif1;
ybdf=1.9*K_s*K_hc*(5/(1+fci))*td^-0.118*K_tddf;
ydf=1.9*K_sd*K_hc*(5/(1+fcd))*ti^-0.118*K_tdddf;
Kid=1./(1+ni*alpha_net*Aps/Anet*(1+.7*ybif));
Kdf=1./(1+ni*alpha_comp_net*Aps/A_comp_net*(1+.7*ybif));
e_bid=.00048*(5/(1+fci))*K_s*K_hs*K_tdid;
e_ddf=.00048*(5/(1+fcd))*K_sd*K_hs*K_tdddf;
e_bif=.00048*(5/(1+fci))*K_s*K_hs*K_tddf;
e_bdf=e_bif-e_bid(1,length(e_bid));
fcgp=fpi*Aps*(1/Atr+(ep.^2./Itr))-(M.*ep./Itr);
for i=1:1:length(ybid)
    for m=1:1:11;
delta_fp_cr(i,m)=ni*fcgp(1,m)*ybid(1,i)*Kid(1,m); %#ok<AGROW>
    end
end
for i=1:1:length(e_bid)
    for m=1:1:11
        delta_fp_sr(i,m)=e_bid(1,i)*Es*Kid(1,m); %#ok<AGROW>
    end
end
for i=1:1:td-ti+1
    for m=1:1:11
delta_fp_r(i,m)=1.2; %#ok<AGROW>
    end
end
loss_id=delta_fp_r+delta_fp_cr+delta_fp_sr;
for i=1:1:td
    for m=1:1:11
        curv_id(i,m)=-
loss_id(i,m)*Aps*ep_tr_final(1,m)/Itr_final(1,m)/Eci; %#ok<AGROW>
    end
end
Wdeck=((t*width)+(ha_t*ha_w))/144*.15;
Mdeck=Wdeck/2*(L*x-x.^2)*12;
Madl=[0.00  0.00  0.00  0.00  0.00  0.00  0.00  0.00  0.00  0.00
      0.00];
curv_deck=-Mdeck/Ec./Itr_final;
for i=1:1:length(curv_id)
    did(:,i)=defl*curv_id(i,:)';  %#ok<AGROW>
end
z=zeros(length(curv_id),1);
camber_id=[z did' z];
for i=1:1:length(camber_id)
    for m=1:1:11

camber_at_deck(i,m)=camber_rel(1,m)*(1+ybid(1,i))+camber_id(i,m)*(1+0.7
*ybid(1,i));  %#ok<AGROW>
    end
end
defl_due_deck=defl*curv_deck';
camber_deck=[0 defl_due_deck' 0];
camber_net_deck=camber_at_deck(length(camber_at_deck),:)+camber_deck;
time=0:1:td-1;
camber_at_deck(length(camber_at_deck),:)=camber_net_deck;
for i=1:1:length(K_tdddf)
    for m=1:1:11
        SR_deck(i,m)=-
n*e_ddf(1,i)*t*width*Ecd/(1+0.7*ydf(1,i))*((1/A_comp_net)+(ep_comp_net(
1,m)*ed_comp_net(1,m))/I_comp_net(1,m)); %#ok<AGROW>
    end
end
for i=1:1:length(e_bdf)
    for m=1:1:11
```

```
        SR_bdf(i,m)=-e_bdf(1,i)*Es*Kdf(1,m); %#ok<AGROW>
    end
end
for i=1:1:length(ybif1)
    for m=1:1:11
        CR_df(i,m)=-ni*fcgp(1,m)*(ybif1(1,i)-
ybid(1,length(ybid)))*Kdf(1,m); %#ok<AGROW>
    end
end
longterm_id=-loss_id(length(loss_id),:)*Aps.*alpha_net/Anet;
k57=-Mdeck.*ep_tr_final./Itr_final-Madl.*ep_comp_tr./I_comp_tr;
sum=longterm_id+k57;
for i=1:1:length(ybdf)
    for m=1:1:11
        CR_b(i,m)=-n*sum(1,m)*ybdf(1,i)*Kdf(1,m); %#ok<AGROW>
    end
end
longterm_df=CR_b+CR_df+SR_bdf+SR_deck-1.2;

for i=1:1:length(longterm_df)
    for j=1:1:11
curv_longterm(i,j)=longterm_df(i,j)*Aps*ep_comp_net(1,j)/I_comp_net(1,j
)/Ec; %#ok<AGROW>
    end
end
for i=1:1:length(curv_longterm)
    def_longterm(:,i)=defl*curv_longterm(i,:)'; %#ok<AGROW>
end
z1=zeros(length(def_longterm),1);
camber_longterm=[z1 def_longterm' z1];
curv_dl_comp=-Madl./I_comp_tr/Ec;
dfl_due_dl_comp=defl*curv_dl_comp';
camber_dl_comp=[0 dfl_due_dl_comp' 0];
for i=1:1:length(camber_longterm)
    for j=1:1:11

camber_final(i,j)=(camber_rel(1,j)*(1+ybif1(1,i)))+(camber_id(length(ca
mber_id),j)*(1+0.7*ybif1(1,i)))+(camber_deck(1,j)*(1+ybdf(1,i)))+(cambe
r_dl_comp(1,j)*(1+ybdf(1,i)))+(camber_longterm(i,j)*(1+.7*ybdf(1,i)));
    end
end
camber_if=[camber_at_deck; camber_final];
time_final=[time td:1:tf-1];
figure(2)
plot(time,camber_at_deck(:,6)');grid on
xlabel('Beam Age (d)')
ylabel('Camber (in)')
title('Midspan Camber, initial to deck placement')
figure(3)
plot(x,camber_net_deck);grid on
xlabel('Length (ft)')
ylabel('Camber (in)')
title('Net Camber after deck placement')
total_camber=[camber_at_deck; camber_net_deck];
figure(4)
plot(time,camber_at_deck(:,6));grid on
xlabel('Beam Age (d)')
ylabel('Camber (in)')
title('Midspan Camber, initial to deck placement')
figure(5)
plot(time_final,camber_if(:,6)');grid on
xlabel('Beam Age (d)')
ylabel('Camber (in)')
title('Midspan Camber, initial to final*')
```